Characterisation of uncertainties in an ocean radiative transfer model for the Black Sea through ensemble simulations

Loïc Macé[1][2], Luc Vandenbulcke[1], Jean-Michel Brankart[2], Pierre Brasseur[2], and Marilaure Grégoire[1]

[1]FOCUS-MAST research group, Department of Astrophysics, Geophysics and Oceanography, University of Liège, Belgium
[2]Univ. Grenoble Alpes, CNRS, INRAE, IRD, Grenoble INP, IGE, Grenoble, France

Correspondence: Loïc Macé (loic.mace@uliege.be)

Abstract.

In this paper, we investigate the influence of uncertainties in inherent optical properties on the modelling of radiometric quantities by an ocean radiative transfer model, in particular irradiance and reflectance. The radiative transfer model is coupled to a three-dimensional physical-biogeochemical model of the Black Sea. It describes the vertical propagation of incident irradiance within the water column along three streams in downward (direct and diffuse) and upward directions, with a spectral resolution of 25 nm in the visible range. The propagation of irradiance streams is governed by the inherent optical properties of four major optically active constituents found in seawater and provided by the biogeochemical model: pure water, phytoplankton, non-algal particles and coloured dissolved organic matter. Sea surface reflectance is then derived as the ratio between the simulated upward and downward irradiance streams, directly connecting the model with remote-sensed data. In this configuration, the coupling is one-way: the radiative transfer model is projecting model variables into the space of satellite observations, working as an observation operator. In the stochastic version of the model, uncertainties are injected in the form of random perturbations of the inherent optical properties of the water constituents. Different ensemble configurations are derived and their quality is assessed by comparison with *in situ* and remote-sensed observations.

We find that the modelling of the uncertainties in the radiative transfer model parametrisation allows to simulate distributions of radiative fields that are partially consistent with observations. The ensemble is consistent with remote-sensed reflectance data in summer and autumn, especially in the central parts of the basin. The quality of the ensemble is lower in winter and early spring, suggesting the existence of another major source of uncertainty or that the quality of the deterministic solution is insufficient. CDOM dominates absorption in short wavebands with a relatively high uncertainty that influences irradiance and reflectance outputs. This dominant role calls for better representation of CDOM to improve model calibration. Contributions from phytoplankton and non-algal particles are more significant for (back-)scattering. The results of this paper suggest that the integration of a radiative transfer model into a physical-biogeochemical model would be beneficial for calibration, validation, and data assimilation purposes, offering a better link between model variables and radiometric observations.

1 Introduction

The spectral distribution of light in the ocean is closely linked to biological activity, biogeochemical cycles, and upper ocean physics (Mobley et al., 2015). The biological productivity of the ocean is directly controlled by the amount of light available to phytoplankton for photosynthesis (Kettle and Merchant, 2008; Gregg and Rousseaux, 2016). The spectral range for photosynthetically active radiation (PAR) corresponds ~~mostly~~ mainly to the visible range and represents about 45% of the total incident radiation at sea surface. Upon reaching the ocean surface, a small part of the incoming radiation is directly reflected depending on the surface albedo. The rest of the solar irradiance is transmitted to the ocean and its vertical spectral distribution is determined by the optical properties of seawater components such as water molecules, dissolved and particulate materials of various sizes and living material (Mobley et al., 2015). The characterisation of those properties is therefore essential. Marine optics also influences temperature, as most of the absorbed irradiance is converted into energy to heat up the water column (Baird et al., 2020). Those processes participate in modifying the upper ocean stratification and turbulence, thus influencing the distribution of optically active components close to the ocean surface. As such, a bio-optical feedback exists between phytoplankton, upper ocean physics and surface circulation ~~(Fujii et al., 2007; ?; Cahill et al., 2023)~~ (Fujii et al., 2007; Cahill et al., 2008, 2023; Skákala et al., 2022).

Optically active constituents are defined by their ability to absorb and scatter radiation, called inherent optical properties (IOPs). IOPs depend on the medium and are independent ~~from~~ of the ambient light field. They ~~consist in~~ can be described by the absorption and (back-) scattering spectra ~~for~~ of each water constituent. The determination and ~~parameterisation~~ parametrisation of IOPs are a major challenge in modelling coupled ~~physical-bio-optical~~ physical and bio-optical processes (Manizza et al., 2005; Werdell et al., 2018). Most of the vertically resolved biogeochemical models solve only the direct downward component of light in a one-stream model, with a single equation describing the decrease in irradiance with depth following Beer's law ~~(?)~~(e.g. Lengaigne et al., 2007), in a limited number of spectral bands~~,~~ usually two or three. They ~~usually~~ differentiate the red ~~from~~ part from the rest of the visible range, which is further separated in some cases between the ~~visible part which, in some cases, is separated in the~~ blue and green wavebands ~~(Aumont et al., 2015; Butenschön et al., 2016; ?)~~ (Aumont et al., 2015; Butenschön et al., 2016). The absorption and (back-)scattering processes are then not distinguished and are merged within a more general attenuation coefficient to represent the attenuation of light over the water column. Over the years, ~~various~~ models were developed with different approaches to refine the representation of light ~~in models (Gregg and Casey, 2009; ?)~~ (Ackleson et al., 1994; Bissett et al., 1999; Gregg and Casey, 2009; Mobley, 2011).

Remote-sensed optical observations rely on passive radiometers to measure top-of-atmosphere radiance in the visible and near infrared bands. Then, the use of atmospheric corrections allows to estimate water-leaving irradiance to compute remote sensed reflectance (R_{RS}) in several wavebands. In units of ~~sr^{-1}~~ sr^{-1}, R_{RS} is a measure of the water-leaving irradiance normalised by the above water downwelling irradiance. To compare this data with biogeochemical variables, inversion ocean colour algorithms compute intermediate products such as surface chlorophyll from reflectances in selected wavebands. These

algorithms remain rather uncertain, and a more straightforward use of reflectance would mitigate the influence of imperfect

60 inversion algorithms. However, a one-stream optical model does not simulate the upward irradiance and thus cannot provide estimates of sea surface reflectance. ~~Limited use has been made~~ So far, limited use of optical properties ~~so far~~ has been made in data assimilation (Ciavatta et al., 2014; Jones et al., 2016), which could change with recent hyperspectral sensors such as those of the PRISMA and PACE missions. In recent years, new optical models have emerged to fill this gap and resolve sea surface reflectance (Dutkiewicz et al., 2015). Some of these models resolve three streams of irradiance by considering scattered

65 irradiance in both downward and upward directions, with higher spectral resolution matching the measured wavebands. As a three-stream optical model adds complexity to coupled modelling frameworks, it also becomes necessary to assess the relative uncertainties in the information produced by the model and by satellite sensors.

In this paper, we couple a 3D ocean physical-biogeochemical model implemented in the Black Sea with a radiative transfer

70 (RT) model as previously used in a global setup ~~(Dutkiewicz et al., 2015)~~ as in Dutkiewicz et al. (2015). The RT model describes the in-water irradiance along the vertical and in three streams: direct downward, diffuse downward and diffuse upward. ~~It solves the spectral~~ Its spectral range includes the wavebands corresponding to those typically used in remote sensing (e.g. 412, 490 or 555 nm). The penetration of ~~the~~ spectral irradiance is determined in 33 wavelengths by the absorption and scattering properties of the medium that are derived from concentrations of optically active components~~, in 33 wavelengths. Following~~

75 . According to the literature, four main optically active elements are considered: water molecules, phytoplankton, non-algal particles and coloured dissolved organic matter (CDOM). Based on the simulated irradiance streams, the RT model is used to estimate sea surface reflectance. Then, we combine the ~~model derived~~ model-derived reflectances in selected wavebands to obtain an estimation of surface chlorophyll, as it is done in satellite inversion algorithms. With this approach using reflectance-derived chlorophyll, the difference between model and satellite estimated chlorophyll is reduced thanks to the common use of

80 empirical inversion algorithms. Dutkiewicz et al. (2018) presented a proof of concept for the use of a new estimate of chlorophyll (they introduce a proxy for chlorophyll called "derived chlorophyll a"), ~~inquiring~~ enquiring on the opportunities provided by the use of RT within a coupled biogeochemical framework. They found that this proxy compared better to measurements ~~that~~ than the "actual" chlorophyll from their biogeochemical model, with better performances using region-specific methods rather than a global method. In this paper, we use a similar proxy in the Black Sea to evaluate its potential use in this region.

85 We also aim at building up from their work by analysing more thoroughly the inner operation of the RT model with regard to the propagation of uncertainties in such a framework. Here, we focus on the deep sea, where BGC-Argo data ~~are available to derive CDOMestimation. Results~~ is available to estimate the contribution of CDOM. Due to a lack of information on CDOM in the shelf region, the results presented in this paper are mainly valid for the ~~deep region and not for the shelf for which we lack information on CDOM~~ deeper parts of the Black Sea (Grégoire et al., 2023).

90

By perturbing the IOPs of the four selected water constituents, we also aim to use this implementation to assess the intrinsic uncertainty of the RT model. An ensemble simulation strategy is set up to inject perturbations in the IOPs and evaluate their

influence on the outputs of the RT model: irradiance and sea surface reflectance. ~~We first assess~~ This analysis comes in three steps:

95
1. Assessment of the effect of ~~uncertainty in the parameterisation~~ uncertainties in the parametrisation of absorption and (back-)scattering for ~~constituents separately. Then, we estimate~~ each constituent separately.

2. Estimation of the combined effect of uncertainties for all uncertain constituents on irradiance and reflectance fields~~, and evaluate to what extent the modelling of uncertainties can help in providing distributions of~~.

3. Evaluation of our ability to provide distributions of sea surface reflectance that are consistent with observations ~~.~~ by
100
    modelling these uncertainties.

To focus the analysis on the RT model, we use it as an observation operator. The RT model takes information from the biogeochemical model without feeding back to the hydrodynamics and biogeochemistry models, and therefore does not influence temperature and primary production.

105
The following section presents the deterministic coupled modelling framework and the ~~parameterisation~~ parametrisation of the optically active components available in the RT model. Section 3 describes the stochastic modelling approach and the introduction of uncertainties within the RT equation. In section 4, we describe the ensemble simulations and results, investigating the impact of uncertainties and the ability of the model to produce relevant surface reflectance distributions. ~~A discussion is finally proposed~~ Finally in section 5, ~~along with possible~~ we discuss the assumptions and limitations of the study, and provide
110
an outlook for future ~~explorations~~ work.

2   Deterministic modelling framework

In this section, we describe the modelling framework and the observations used for ~~the validation of the system~~ system validation. A schematic description of the modelling framework, the diagnostics provided by the RT model and the relevant
115
observations (detailed ~~further~~ in section 4) are presented in Fig. 1. The deterministic model couples a physical-biogeochemical model for the Black Sea with a three-stream RT model. Gathering information from the biogeochemical and hydrodynamics models (section 2.1), the three-stream RT model (subsection 2.2) computes fields of irradiance and sea surface reflectance. These can be compared to both *in situ* and remote-sensed data (section 2.3). The required inputs to perform this operation are provided both by the NEMO-BAMHBI system for IOPs (section 2.4), and forced from ~~MAR atmospheric forcing~~ simulation
120
outputs from a MAR regional atmospheric configuration (section 2.5) for above water irradiance.

2.1   Physical-biogeochemical coupled system NEMO-BAMHBI

The physical-biogeochemical coupled system NEMO-BAMHBI is implemented within the Black Sea Monitoring and Forecasting system of the ~~Black Sea~~ Copernicus Marine Service. The hydrodynamics are solved with NEMO 4.2 ~~and~~ which is online
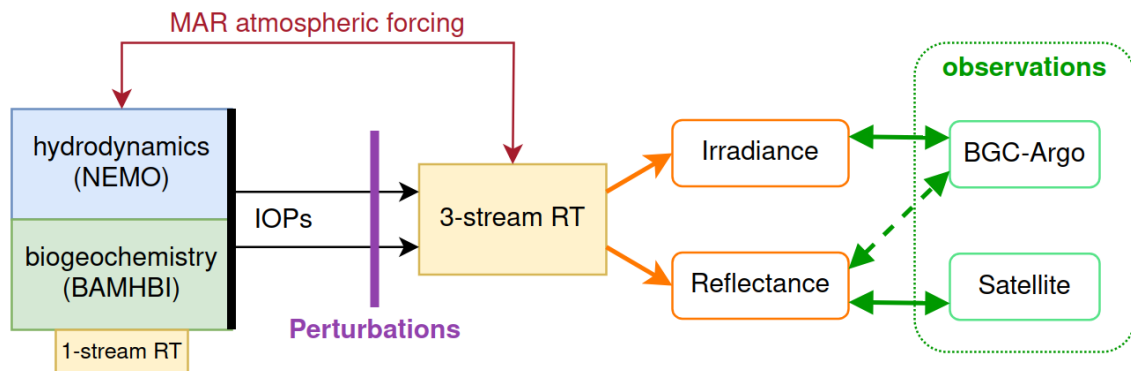
Figure 1. Coupled NEMO-BAMHBI modelling framework with the 3-stream RT model functioning in one-way coupling. The RT model is used as an observation operator, projecting model variables into the space of observations. Since it does not feed back to NEMO-BAMHBI, a simple one-stream RT model is kept to compute temperature. Among the outputs of the RT model, irradiance is compared to BGC-Argo data, reflectance is compared to remote-sensed data and BGC-Argo data, through inversion algorithms used to retrieve surface chlorophyll.

coupled ~~with~~ to the biogeochemical model. BAMHBI (Biogeochemical Model for Hypoxic and Benthic Influenced areas) is

125 a biogeochemical model that describes the biogeochemical cycles of carbon and nitrogen through the food web~~going~~, from bacteria up to mesozooplankton ~~(Grégoire et al., 2008; Grégoire and Soetart, 2010; ?)~~(Grégoire et al., 2008; Grégoire and Soetart, 2010; Cape
. It explicitly represents processes in the anoxic layer, with a 28-variable pelagic component (including the carbonate system) and a 6-variable benthic component.

130 The default light penetration scheme used in BAMHBI is a one-stream (i.e. direct downward) RT scheme in three wavebands: two in the visible range and one in the infrared. The sea surface radiation is computed using astronomical forcing to estimate the radiance at the top of the atmosphere and is propagated to the sea surface using the cloud cover data from a regional atmospheric model (MAR) run for the Black Sea. The sea surface radiation is then attenuated with depth following Beer's law with attenuation derived from concentrations of biogeochemical variables: pure water, phytoplankton, suspended

135 minerals and CDOM. This simple RT model is then used to derive PAR, and the amount of irradiance absorbed is a source term in the equation of conservation of thermic energy in NEMO.

In operational and reanalysis mode, the coupled model works with a horizontal resolution of 2.5 km and 59 unevenly distributed vertical levels, with thinner layers close to the surface and the pycnocline. ~~In~~ However, in this study, we use a

140 horizontal resolution of 15 km ~~and~~ with the same vertical levels. ~~A~~ The reduced horizontal resolution is chosen here ~~in order~~ to minimise computational costs ~~, especially in light of ensemble runsthat are described in Section 3.~~ for ensemble runs. In the configuration used in this study, we use a velocity forcing as a boundary condition at the Bosphorus strait for exchanges with the Mediterranean Sea, as described in Stanev and Beckers (1999). It is assumed that there are no exchanges with the Azov Sea. River runoffs and atmospheric deposition of nutrients (phosphorus, nitrate and ammonium) are based on climatology.

145 ~~Initial~~ The initial conditions for the simulations performed in this study are taken from a longer stable run in a similar model configuration.

2.2 The radiative transfer observation operator

The one-dimensional 3-stream RT model is directly inspired ~~from~~ by the model described in Dutkiewicz et al. (2015) within the ~~frame~~ framework of the global MITgcm model. Three streams of irradiance are computed based on the absorption and (back-
150)scattering properties of the medium: a downward direct irradiance (Ed E_d) that accounts for transmitted light, a downward scattered irradiance (Es E_s) that accounts for light that has been scattered in the forward direction, and an upward irradiance (Eu E_u) that accounts for ~~the~~ light that has been backscattered towards the ocean surface. Resolving the three irradiance streams allows for comparison with remote-sensed data thanks to the computation of the upward E_u stream at the surface, while the downward E_d and E_s streams are a decomposition of the single stream found in one-stream RT models.
155

The RT model simulates irradiance streams in 33 wavebands ranging between 250 and 4000 nm, with a finer 25 nm resolution in the visible range. This operator is one-dimensional and therefore processes each water column individually. On the vertical, we consider that all scattering happens only either forwards or backwards. We only represent elastic scattering, assuming that inelastic scattering processes are of lower magnitude. ~~Attenuation coefficients are declined into~~ The attenuation coefficients
160 are derived from absorption (a), scattering (b) and backscattering (b_b) coefficients, all in units of m^{-1}. The propagation of light in the water column is then described by the following system of equations:

$$\frac{dE_d(\lambda)}{dz} = -\frac{a(\lambda) + b(\lambda) + b_b(\lambda)}{\overline{v_d}} E_d(\lambda) \tag{1}$$

$$\frac{dE_s(\lambda)}{dz} = -\frac{a(\lambda) + r_s b_b(\lambda)}{\overline{v_s}} E_s(\lambda) + \frac{r_u b_b(\lambda)}{\overline{v_u}} E_u(\lambda) + \frac{b(\lambda)}{\overline{v_d}} E_d(\lambda) \tag{2}$$

$$-\frac{dE_u(\lambda)}{dz} = -\frac{a(\lambda) + r_u b_b(\lambda)}{\overline{v_u}} E_u(\lambda) + \frac{r_s b_b(\lambda)}{\overline{v_s}} E_s(\lambda) + \frac{b_b(\lambda)}{\overline{v_d}} E_d(\lambda) \tag{3}$$

165 where r_s and r_u are dimensionless normalised effective scattering coefficients, and $\overline{v_d}, \overline{v_s}, \overline{v_u}$ are average cosines accounting for the angle of incidence of light, also dimensionless (Aas, 1987). These coefficients are approximated with constant values and detailed in ~~Table~~ Tab. 1. This system is closed for each water column with two surface conditions provided by the radiative forcing on E_d and E_s, and one bottom condition imposing E_u to ~~be~~ 0. ~~PAR is then~~

170 We define PAR as the total irradiance in the visible range, scaled by the angular coefficients $\overline{v_d}$, $\overline{v_s}$ and $\overline{v_u}$. Although the PAR simulated by the RT model is not used in the coupled framework in a one-way configuration, it is a useful quantity that can be used for comparison with *in situ* data. In units of W/m^2, it is derived with:

$$PAR = \int\limits_{400nm}^{700nm} \left[\frac{E_d(\lambda)}{\overline{v_d}} + \frac{E_s(\lambda)}{\overline{v_s}} + \frac{E_u(\lambda)}{\overline{v_u}} \right] d\lambda \tag{4}$$

We then define the sea surface reflectance R in the upper layer $z = 0$ (below surface) based on the three streams of irradiance as follows:

$$R(\lambda, 0^-) = \frac{E_u^{z=0}(\lambda)}{E_d^{z=0}(\lambda) + E_s^{z=0}(\lambda)} \tag{5}$$

The simulated reflectance is not strictly the same quantity as the remote-sensed reflectance R_{RS} which is estimated above the sea surface. Following Dutkiewicz et al. (2018), two corrections are made to make the modelled reflectance comparable to R_{RS} satellite measurements. The subsurface reflectance is first adjusted so that the upwelling irradiance stream E_u is transformed into upwelling radiance as seen by satellite instruments. This transformation is performed according to the bidirectional reflectance distribution function (BRDF) of the ocean surface. The BRDF depends on many variables such as the wave state at the surface, the solar zenith angle and the optical properties at the air-sea interface (Morel et al., 2002). It is simplified here in a constant coefficient Q. Q is generally estimated between 3 and 6 sr. In this study, we set Q to 4.5 sr.

$$R_{RS}^{below}(\lambda, 0^-) = \frac{R(\lambda, 0^-)}{Q} \tag{6}$$

An additional correction is performed to account for interface effects. It aims to translate subsurface remote-sensed reflectance to above-surface remote-sensed reflectance following Lee et al. (2002).

$$R_{RS}(\lambda, 0^+) = \frac{0.52 R_{RS}^{below}(\lambda)}{1 - 1.7 R_{RS}^{below}(\lambda)} \tag{7}$$

$R_{RS}(\lambda)$ is now directly comparable to remote-sensed reflectance data. Among the available satellite products, we will be using here the multi-satellite product provided by the Copernicus Marine Service for the Black Sea for validation and comparison. It combines measurements from the Sentinel-3A, Sentinel-3B, Aqua, Suomi NPP and JPSS-1 satellites. This L3 product is available from 1997 and provides daily measurements of sea surface reflectance with a horizontal resolution of 1 km, in 6 wavebands centred on 412, 443, 490, 510, 555 and 670 nm.

2.3 Ocean colour algorithms

Ocean colour algorithms are used to estimate surface chlorophyll from sea surface reflectance. In the Black Sea, the Copernicus Marine Service uses a merged product between two algorithms: a band-ratio algorithm and a neural network based method (Zibordi et al., 2015). The neural network is used primarily for complex waters such as coastal areas of the northwestern continental shelf of the Black Sea. The blue/green band-ratio algorithm is based on reflectances in

Table 1. Average cosines and normalised effective scattering coefficients used in RT equations.

Parameter	Value	Unit
$\overline{v_d}$	1.5	[-]
$\overline{v_s}$	0.83	[-]
$\overline{v_u}$	0.4	[-]
r_s	1.5	[-]
r_u	3	[-]
Q	4.5	1/sr

200   the 490 and 555 nm wavebands and is used to derive an estimate of surface chlorophyll (Kajiyama et al., 2018). We choose to reproduce the band-ratio algorithm to derive an estimate of surface chlorophyll based on the reflectances simulated in the RT model (Dutkiewicz et al., 2018). This choice over the neural network approach is motivated by our focus on the deep parts of the basin, where the band-ratio algorithm is predominantly used. In the following, we call this reflectance-derived chlorophyll estimate ~~rCHL~~ $rCHL$:

$$log(rCHL) = \sum_{k=0}^{3} c_k \times \left[log\left(\frac{R_{RS}(490)}{R_{RS}(555)} \right) \right]^k \tag{8}$$

The algorithm described in Kajiyama et al. (2018) provides the c_k coefficients for the ~~Western~~ western Black Sea. We choose here to expand this formulation ~~for~~ to the entire basin. This new estimate is not independent ~~from~~ of the chlorophyll simulated in BAMHBI since outputs of BAMHBI intervene in the simulation of reflectances, but provides a quantity that corresponds more closely to satellite chlorophyll products. From the perspective of modelling, using a reflectance ratio is also interesting as it removes the uncertainty that arises from the simplification of BRDF.

2.4   Optically active components

The absorption and scattering of light by seawater are modelled as the linear combination of individual contributions from pure water, phytoplankton, non-algal particles and CDOM. Sources from literature for specific coefficients used ~~and IOPs~~ to derive each contribution are summarised in Tab. 2. In the following, the subscripts "w", "phy", "prt" and "cdom" denote their respective contributions. We assume here that CDOM only participates in absorption and not in scattering ~~(Dutkiewicz et al., 2015; Álvarez et al., 2023)~~ as in Dutkiewicz et al. (2015) and Álvarez et al. (2023).

$$a(\lambda) = a_w(\lambda) + a_{phy}(\lambda) + a_{prt}(\lambda) + a_{cdom}(\lambda) \tag{9}$$

$$b(\lambda) = b_w(\lambda) + b_{phy}(\lambda) + b_{prt}(\lambda) \tag{10}$$

$$b_b(\lambda) = b_{b.w}(\lambda) + b_{b.phy}(\lambda) + b_{b.prt}(\lambda) \tag{11}$$

2.4.1 Water

The absorption and scattering properties of water (a_w, b_w and $b_{b.w}$) ~~are considered~~ have been well documented by ~~many laboratory experiments (Pope and Fry, 1997; Morel et al., 2007)~~ laboratory experiments (Pope and Fry, 1997; Morel et al., 2007; Mason et . Water is an important constituent with a very high absorbing power in the infrared and ultraviolet, ~~but rather low in the PAR and lower in the visible~~ range. Scattering by water is considered isotropic ~~meaning that, ,~~ meaning that in 1D, $b_w = b_{b.w}$. Absorption and scattering spectra for water in the visible range are provided in Fig. 2, with ~~increasing absorption with wavelength and decreasing scattering~~ higher absorption and lower scattering for longer wavelengths.

2.4.2 Phytoplankton and non-algal particles

Absorption and (back-)scattering by phytoplankton (a_{phy}, b_{phy} and $b_{b.phy}$) are modelled as the sum of individual IOPs for each phytoplankton functional type (PFT) solved in BAMHBI: these are large flagellates (representative of dinoflagellates), small flagellates (representative of coccolithophores) and diatoms ~~; that~~, all of which are the dominant species in the Black Sea (Silkin et al., 2021). ~~Specific~~ The specific absorption and (back-)scattering coefficients associated ~~to~~ with phytoplankton are adapted from Álvarez et al. (2022) to the PFTs modelled in BAMHBI. Specific coefficients for absorption (a_{phy}^i) have units of m²/mgChl while specific coefficients for scattering (b_{phy}^i and $b_{b,phy}^i$) have units of m²/mmolC.

$$a_{phy}(\lambda) = \sum_i a_{phy}^i(\lambda) CHL^i \tag{12}$$

$$b_{phy}(\lambda) = \sum_i b_{phy}^i(\lambda) C_{chl}^i \tag{13}$$

$$b_{b,phy}(\lambda) = \sum_i b_{b,phy}^i(\lambda) C_{chl}^i \tag{14}$$

where CHL^i is the chlorophyll concentration for each PFT in units of mgChl/m³ and C_{chl}^i is the carbon content in each PFT in units of mmolC/m³. Specific absorption and scattering spectra for phytoplankton are provided in Fig. 2.

Similarly, IOPs of non-algal particles (a_{prt}, b_{prt} and $b_{b.prt}$) are derived from specific coefficients (respectively a_{prt}^0, b_{prt}^0 and $b_{b,prt}^0$) from Gallegos et al. (2011) and Álvarez et al. (2022). The computation of these coefficients ~~rely~~ relies on the
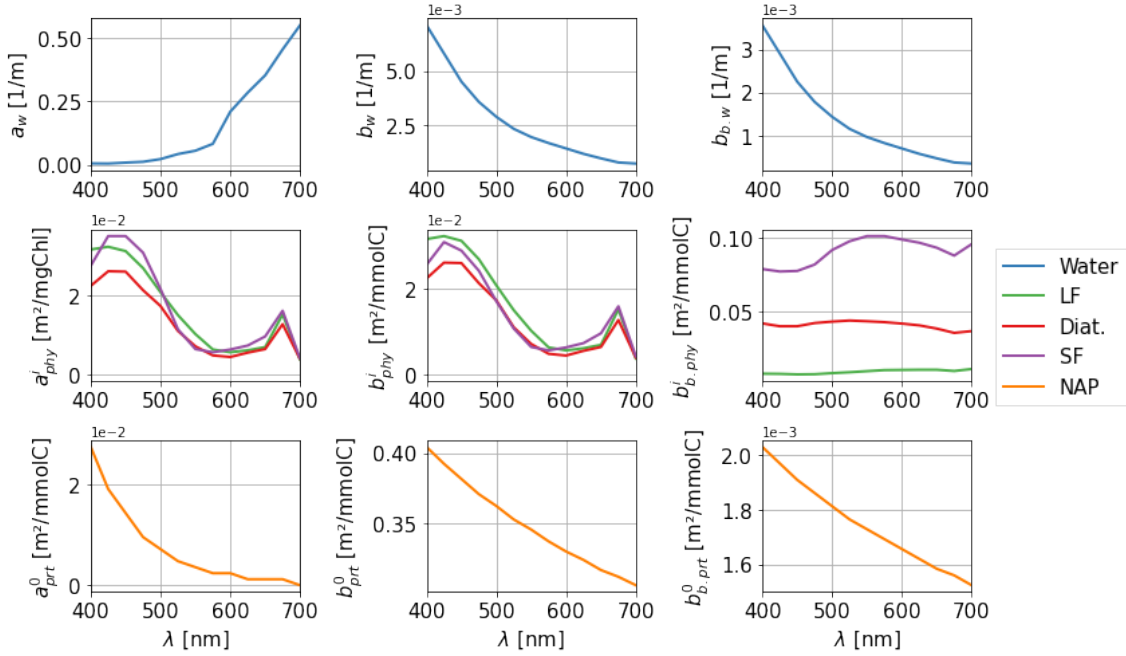
Figure 2. IOPs for water (a_w, b_w and $b_{b.w}$) (top), phytoplankton (a_{phy}^i, b_{phy}^i and $b_{b,phy}^i$) (~~middle~~centre) and non-algal particles (NAP) (a_{prt}^0, b_{prt}^0 and $b_{b,prt}^0$) (bottom). The three PFTs represented here are large flagellates (LF), diatoms (Diat.) and small flagellates (SF). Spectral resolution in the model is 25 nm in the visible range (400-700 nm).

use of particulate organic carbon (POC; computed dynamically in BAMHBI) as a proxy for particle concentration, assuming uniformity in the size and distribution of particles as in Dutkiewicz et al. (2015). Specific absorption and scattering spectra for particles are provided in Fig. 2.

$$a_{prt}(\lambda) = a_{prt}^0(\lambda)POC \tag{15}$$

$$b_{prt}(\lambda) = b_{prt}^0(\lambda)POC \tag{16}$$

$$b_{b,prt}(\lambda) = b_{b,prt}^0(\lambda)POC \tag{17}$$

2.4.3 CDOM

Although CDOM is a major contributor to irradiance absorption within the water column, ~~CDOM~~ it is not explicitly simulated in the NEMO-BAMHBI framework. We choose here to derive a forcing for a_{cdom} from a collection of BGC-Argo ~~irradiance~~ profiles. The RT model is run by deriving IOPs from BGC-Argo data to reproduce irradiance ~~profile~~ profiles at a reference wavelength $\lambda_{ref} = 412$ nm by optimising a_{cdom} to fit the measured profiles. The description of data, the setup and detail of
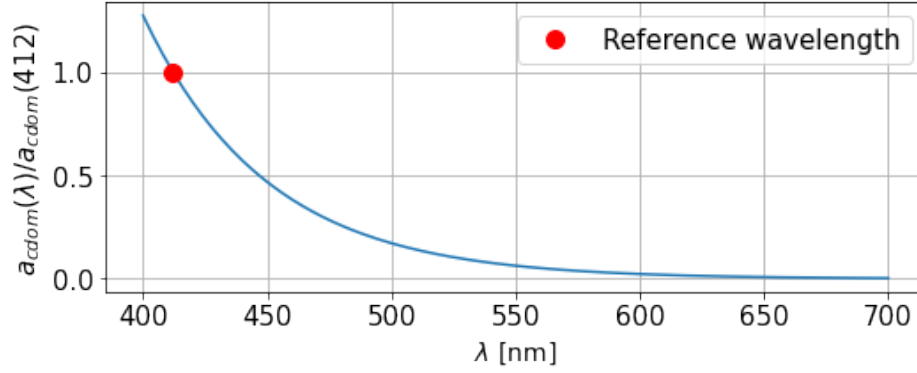
Figure 3. Absorption spectrum for CDOM as the ratio with absorption at the reference wavelength $\lambda_{ref} = 412$ nm.

the method of this experiment are presented in Appendix A.

The forcing for $a_{cdom}(\lambda_{ref})$ depends on time and seawater density ρ as a way ~~of accounting~~ to account for ocean physics and spatial and seasonal variability. It also accounts for the increase in CDOM, and therefore in a_{cdom}, with depth. This approach is not valid in coastal areas and on the continental shelf, where we observe low densities due to large ~~river discharges of freshwater~~ freshwater discharges from rivers. With this method, low density areas are associated with low CDOM, which goes against the high biological activity ~~noticed~~ observed around river estuaries. Since this forcing is generated using data from the central parts of the basin, we acknowledge that it will not be representative of shallow areas. We interpolate this dataset ~~as~~ to generate annual cycles for each density scale.

CDOM is dominant in the blue and decreases for longer wavelengths, parametrised with an exponential law for the absorption coefficient of parameter S_{cdom} (Twardowski et al., 2004; Kitidis et al., 2006; Dutkiewicz et al., 2015). A range of values for this slope is prescribed in Álvarez et al. (2022), and we fit it using BGC-Argo irradiance profiles at 380 and 490 nm in ~~the~~ a benchmark 1D RT model. We use $S_{cdom} = 0.02$ nm^{-1} for our model, leading to the spectrum in Fig. 3. The uncertainty associated ~~to~~ with this extrapolation coefficient will be studied in the next section of the paper. Our forcing for a_{cdom} is finally written:

$$a_{cdom}(\rho,\lambda) = a_{cdom}(\rho,\lambda_{ref})\, e^{-S_{cdom}(\lambda-\lambda_{ref})} \tag{18}$$

2.5 Atmospheric forcing

The ocean model is forced with the outputs of a MAR regional atmospheric model configuration (Gallée et al., 2013). ~~Ran~~ When run over the Black Sea, MAR provides the boundary conditions for ~~the~~ ocean physics: wind velocity, humidity, pre-

Table 2. Specific IOPs for the main water constituents and their references.

$a_w, b_w, b_{b.w}$	1/m	Pope and Fry (1997); Morel (1974)
a_{phy}^i	m^2/mgChl	adapted from Álvarez et al. (2022)
$b_{phy}^i, b_{b,phy}^i$	m^2/mmolC	adapted from Álvarez et al. (2022)
$a_{prt}^0, b_{prt}^0, b_{b,prt}^0$	m^2/mmolC	Gallegos et al. (2011)
a_{cdom}	1/m	calibrated with BGC-Argo data
S_{cdom}	1/nm	calibrated with BGC-Argo data

cipitation, 2 m temperature, mean sea level pressure. The spectral RT model also requires a boundary condition for spectral irradiance. MAR has been extended with a spectral radiative scheme, ecRad, developed by Hogan and Bozzo (2018) to represent the radiative effect of clouds and aerosols in the ECMWF integrated forecasting system. An accurate description of gas optics is also included in the ecCKD tool used in ecRad (Hogan and Matricardi, 2022). Using this extension, MAR provides direct and scattered downward irradiance just above the sea surface in the 33 wavebands selected for the ocean RT model. The irradiance below sea surface is then derived considering surface albedo. The MAR configuration extended with the ecRad scheme is described and validated in Grailet et al. (2025).

In this study, we consider the surface radiative forcing to be accurate and therefore ignore its uncertainty. Although an error in the surface irradiance propagated within the water column, the IOPs would not be altered. Irradiance fields in the water column would be biased due to surface error, but reflectance would not be significantly influenced as it is a variable that is normalised by the incident light. We would therefore obtain very similar results regardless of the surface forcing. This change also would not influence the rest of the NEMO-BAMHBI system in the one-way configuration of the coupled model. The scope of this paper is thus focused on the parametrisation of IOPs in the RT model used as an observation operator.

3   Modelling of uncertainties

In this section, we describe the method we applied to transform the deterministic RT model into a probabilistic model, explicitly simulating the internal sources of uncertainties of the model. Within the RT operator, the IOPs of phytoplankton, non-algal particles and CDOM are uncertain. We aim at quantifying the influence of these uncertainties on the computation of irradiance and reflectance fields. A generic method is presented in this section to perturb IOPs in a similar way for the three constituents.

3.1 Stochastic fields

All stochastic perturbations introduced in the model are produced using the generic approach implemented in the NEMO framework by Brankart et al. (2015) ~~,~~ and subsequently used in the context of coupled physical-biogeochemical modelling by Garnier (2016) and Popov et al. (2024). We start by generating Gaussian processes, characterised by their mean and time-space covariance. The stochastic processes are updated at each time step of the model to simulate the evolution of uncertainties~~in time~~, and correlated in time with a time correlation parameter representative of biogeochemical processes. In our application, we ~~used~~ use first order autoregressive processes (AR1), which means that the value of the process η at time step t_k only depends on η at the previous time step t_{k-1}:

$$\eta(t_k) = \varphi \, \eta(t_{k-1}) + \sqrt{1 - \varphi^2} \, w \tag{19}$$

where w is a random Gaussian noise of mean μ_0 and standard deviation σ_0, and:

$$\varphi = e^{-1/\tau} \tag{20}$$

where w is a normalised white noise (with zero mean and unit standard deviation). With Eq. (19), we can produce AR1 processes with a correlation function given by:

$$corr(\Delta t) = \exp(-\Delta t / \tau) \tag{21}$$

where Δt is the time difference and τ is the decorrelation length scale (both in number of time steps). It represents a decorrelation time at which the influence of a perturbation is $1/e$, and after which it tends to 0. With Eq. (19), we obtain processes with zero mean and unit standard deviation, which can then be rescaled to obtain processes with the required mean (μ_0) and standard deviation (σ_0).

By applying this method independently at each model grid point, we obtain maps of independent stochastic processes that are uncorrelated in space. ~~Space~~ The space correlation is obtained by applying a filtering operator ~~on~~ to the uncorrelated noise. Here, we use a Laplacian filter to generate a perturbation field $\eta^{'}$ from the above time-correlated point-wise time series of perturbations of the 4 neighbouring grid points.

$$\eta^{'}_{i,j}(t_k) = 0.5\eta_{i,j}(t_k) + 0.125(\eta_{i-1,j}(t_k) + \eta_{i+1,j}(t_k) + \eta_{i,j-1}(t_k) + \eta_{i,j+1}(t_k)) \tag{22}$$

where (i,j) is the index of any grid point. This filtering process can be repeated several times to widen the spatial correlation. In this study, this filtering is repeated five times, thus generating a spatial correlation length scale of 75 km (i.e. five times the

Table 3. Time and spatial correlation properties of the stochastic fields generated to perturb IOPs, with standard deviations of each perturbation.

Field	Perturbation	Decorrelation time	Laplacian filtering	σ
η_{phy}	Phytoplankton	30 days	x5	0.5
η_{poc}	Non-algal particles	30 days	x5	0.5
η_{c1}	CDOM absorption at λ_{ref}	30 days	x5	0.5
η_{c2}	CDOM spectral slope	30 days	x5	0.25

spatial resolution of 15 km). The resulting field is normalised again to maintain the required standard deviation.

325

This transformation produces stochastic fields with space and time correlation structures that remain Gaussian. As we want to simulate fields of multiplicative noise, we need random positive numbers. Gaussian processes are thus inappropriate, and we apply an exponential transform to convert the distribution towards a log-normal distribution, noted η''.

$$\eta''_{i,j}(t_k) = e^{\eta'_{i,j}(t_k)} \tag{23}$$

330 The exponential transform of a Gaussian law transforms the mean and ~~the~~ standard deviation of the initial Gaussian distribution. We want the resulting log-normal distribution to have ~~an~~ a unit mean and a standard deviation σ ~~as~~ to generate a spread without introducing bias. This constrains the choice for μ_0 and σ_0 in the initial Gaussian distribution ~~,~~ that are obtained with:

$$\mu_0 = -\frac{\sigma^2}{2} \tag{24}$$
$$\sigma_0^2 = ln(1 + \sigma^2) \tag{25}$$

335 The resulting two-dimensional maps of stochastic fields follow a log-normal distribution of unit mean and standard deviation σ. The time-space correlation structure of these AR1 processes can be tuned with the correlation time scale τ and the number of passes of the horizontal Laplacian filter. In the following, we call ~~η such a~~ this field of perturbation η. These stochastic processes are used as multiplicative noises applied to IOPs in the RT model, with parameters as described in Table 3.

3.2 Uncertainties on phytoplankton and non-algal particles

340 Uncertainties in ~~the~~ IOPs are the joint effect of uncertainties in both the concentrations simulated by BAMHBI and the ~~parameterisation~~ parametrisation of the optical properties (i.e., specific absorption and scattering coefficients) of ~~the optically~~ active components (~~as in~~ Eq. 12 to 17). Since the modelling of the effect of these two sources of uncertainty on the IOPs can be done in a similar way, we consider that perturbing the abundance of the optically active component mimics the effect of uncertainty in both the abundance and ~~parameterisation~~the parametrisation. It should be noted that BAMHBI may miss a

phytoplankton group that is important in the Black Sea, besides the ~~3~~ three PFTs it solves, but this uncertainty is not considered here.

Similarly for non-algal particles, we find uncertainties in both the ~~parameterisation~~ parametrisation of their optical properties and the concentrations. We assume that particles are uniform in size and therefore all share the same specific optical properties. In reality, non-algal particles come in a larger range of sizes and this assumption of uniformity injects uncertainty into the model. Furthermore, the derivation of the particle concentration from POC may also be inaccurate. For both chlorophyll and non-algal particles, the perturbations that are applied are in the form of 2D horizontal fields as described in section 3.1. As such, the perturbation does not modify the vertical structure of the chlorophyll and POC fields, and cannot account for inaccuracy on the depth of chlorophyll or POC maxima.

We choose to model the uncertainties associated ~~to the model abundance~~ with the abundance of optically active components in the model by introducing multiplicative coefficients η_{phy} and η_{poc} ~~to~~ into the computation of absorption and scattering coefficients. The η_{phy} and η_{poc} fields are generated following the method described in section 3.1. As such, chlorophyll and POC concentrations are ~~only perturbed~~ perturbed only at the interface between BAMHBI and the RT model, without influencing the biogeochemical processes described in BAMHBI. Absorption coefficients thus become:

$$a_{phy}^{sto}(\lambda) = \eta_{phy} a_{phy}(\lambda) \tag{26}$$

$$b_{phy}^{sto}(\lambda) = \eta_{phy} b_{phy}(\lambda) \tag{27}$$

$$b_{b,phy}^{sto}(\lambda) = \eta_{phy} b_{b,phy}(\lambda) \tag{28}$$

$$a_{prt}^{sto}(\lambda) = \eta_{poc} a_{prt}(\lambda) \tag{29}$$

$$b_{prt}^{sto}(\lambda) = \eta_{poc} b_{prt}(\lambda) \tag{30}$$

$$b_{b,prt}^{sto}(\lambda) = \eta_{poc} b_{b,prt}(\lambda) \tag{31}$$

$$\tag{32}$$

~~Decorrelation~~ The decorrelation time is set to 30 days consistently with the scale of biogeochemical changes in the Black Sea. Laplacian filtering generates a spatial correlation length scale of approximately 75 km. Finally, the standard deviation is set here to 0.5, based on the ranges of inherent optical properties found in the literature (Gallegos et al., 2011; Dutkiewicz et al., 2015; Álvarez et al., 2022). An example of the resulting field is shown in Fig. 4. The same perturbation field is used for all 59 vertical layers of the model.

3.3 Uncertainty on CDOM

Since CDOM is not explicitly simulated in BAMHBI, its absorption is parametrised from BGC-Argo data. However, ~~this~~ the data does not cover the ~~whole~~ entire basin at all seasons ~~, leading to~~ and we rely on extrapolations to cover the remaining
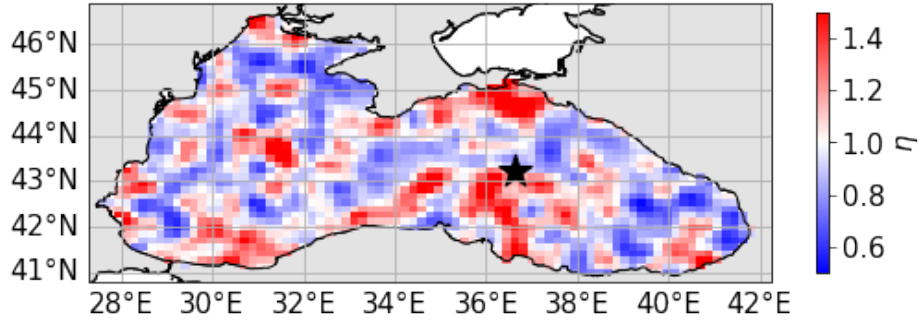
Figure 4. Perturbation field generated according to the method described in section 3.1, following a log-normal distribution with unit mean and standard deviation 0.5, with five passes of Laplacian filtering for space correlation. The black star indicates the location of coordinates 43.22N, 36.63E used in ~~later sections to describe~~ the ~~description of~~ results in this paper.

areas and times. This likely introduces uncertainties in the model, ~~on top of~~ in addition to potential observation errors. The approximation of the CDOM absorption spectrum by a decreasing exponential law may also lead to uncertainties in the representation of CDOM in the RT model, as ~~hinted~~ indicated by the several ranges that can be found in the literature for $~~S_{CDOM}~~$ S_{cdom} (Terzić et al., 2021). Uncertainty ~~on~~ in CDOM absorption is modelled in two steps, perturbing separately the reference absorption profile at 412 nm and the exponential slope of the absorption spectrum, both described in section 2.4.2..

We therefore introduce uncertainty on CDOM absorption in two ways. First~~a~~, a multiplicative factor field η_{c1} ~~field of multiplicative factors~~ is used to perturb the reference absorption coefficient from the reference profile. Then, a η_{c2} field is used to perturb the exponential slope. Both fields are generated according to the method presented in section 3.1.

$$a_{cdom}^{sto}(\rho, \lambda) = \eta_{c1} a_{cdom}(\rho, \lambda_{ref}) \times e^{-\eta_{c2} S_{cdom}(\lambda - \lambda_{ref})} \tag{33}$$

As for chlorophyll and non-algal particles, the decorrelation time is set to 30 days and the spatial correlation length scale to 75 km. ~~Standard~~ The standard deviation for the perturbation of the reference profile is set to 0.5, based on the ranges of CDOM profiles found in the BGC-Argo observations. This standard deviation accounts for the rather simplified representation of spatial and temporal variability in the CDOM concentration and absorption power. ~~Standard~~ The standard deviation for the exponential slope is set to 0.25 based on the range of possible values found in the literature (Terzić et al., 2021). The same perturbation ~~fields~~ field is used for all 59 vertical layers of the model.

4 Ensemble simulations

In this section, we explore the impact of simulating uncertainties as described in section 3 in the modelling framework complemented by the RT model described in section 2. A deterministic reference simulation and 4 distinct ensembles are simulated.

Table 4. Overview of ensembles E1, E2, E3 and E4.

Ensemble	Members	Perturbation of IOPs
E1	10	Phytoplankton
E2	10	Non-algal particles
E3	10	CDOM
E4	20	Combined

395 E1 and E2 ~~each~~ are 10-member ensembles each with perturbations on the optical properties of phytoplankton only and non-algal particles only, respectively, as described in section 3.2. E3 is a 10-member ensemble with perturbations on the optical properties of CDOM only, as described in section 3.3. ~~Both the CDOM absorption reference profile~~ In this ensemble, both the reference profile for CDOM absorption at λ_{ref} and the spectral ~~dependency~~ dependence of CDOM absorption are perturbed~~in this ensemble~~. E4 is a 20-member ensemble combining the perturbations used in E1, E2 and E3 (i.e. on chlorophyll, non-algal

400 particles and CDOM).

All ensemble simulations are performed over 15 months: a spin-up time of 3 months between October and December 2016 followed by the simulation of 2017. The ~~simulated domain covers the entire Black Sea~~ whole Black Sea domain is simulated. 10 members are simulated for ensembles E1, E2 and E3 as few members are deemed enough to evaluate the influence of

405 each perturbation. The most important results described in this section come from ensemble E4, ~~combining~~ which combines perturbations. As such, 20 members were simulated to allow for a more reliable statistical analysis of the ensemble. However, when E4 is directly compared to E1, E2 or E3, it is limited to its first 10 members for consistency.

We begin by studying the individual influence of perturbations on spectral irradiance profiles and surface reflectance. Then,

410 we assess the impact of the combination of uncertainties in E4. Finally, we compare the ensemble results to the observation data to evaluate the ability of the different ensembles to produce distributions that are consistent with the observations.

4.1 Influence of perturbations on radiative transfer

The perturbation of IOPs influences the vertical propagation of irradiance in the water column ~~,~~ by modifying the absorption and (back-)scattering properties of the medium. In the case of CDOM, the perturbation only modifies absorption (see Eq. 1, 2

415 and 3). Modifying the absorption affects the total amount of irradiance propagating in the water column while a modification of the (back-)scattering coefficients affects the direction of light (downward or upward). The three irradiance streams E_d, E_s and E_u are affected by absorption and backscattering. ~~Perturbation~~ The perturbation of scattering coefficients changes the amount of direct irradiance that is scattered ~~,~~ but does not influence the backscattered stream nor reflectance. It also has no influence on the total downwelling irradiance defined as the sum of direct and scattered streams.

420
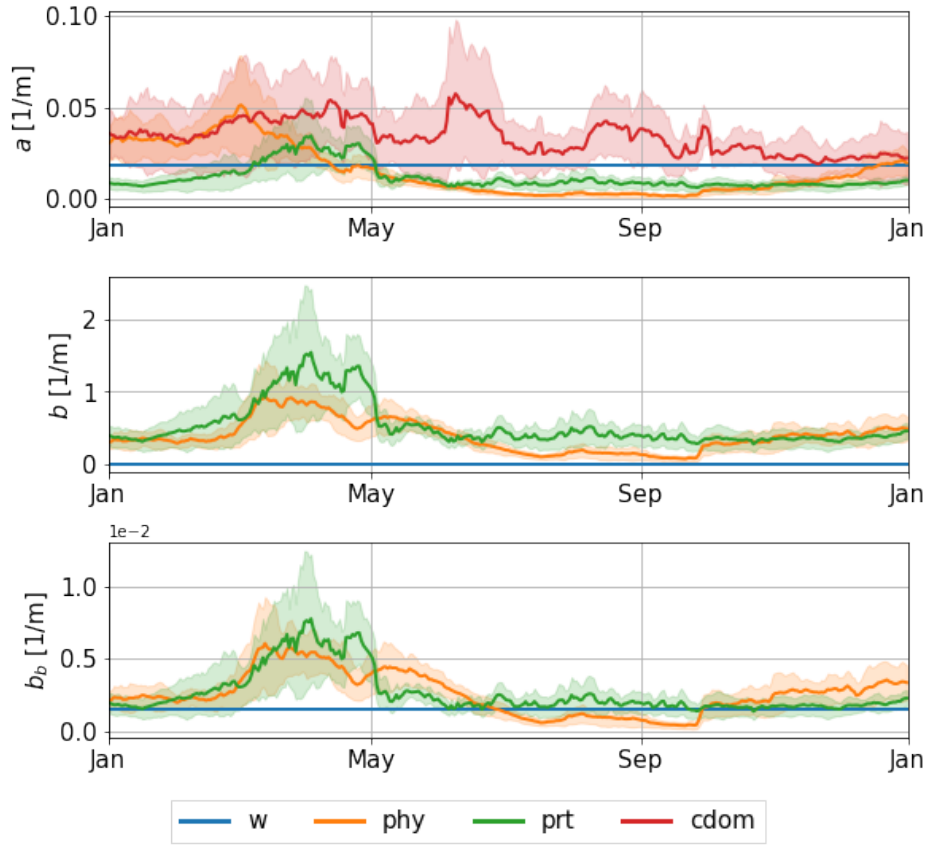
Figure 5. Time series of absorption, scattering and backscattering coefficients at 490 nm from the perturbed runs at 43.22N, 36.63E (see location on Fig. 4) in 2017, at 10.6 m depth. The solid lines represents the ensemble mean and the shaded areas ~~covers~~ cover one standard deviation around the ensemble mean.

The dominant optical constituent for absorption and (back-)scattering varies during the season, region and waveband. In the following, we focus on the spectral bands used in satellite inversion algorithms in the Black Sea to compute surface chloro-phyll: 490 and 555 nm. Appendix B. provides an overview of the model performance in other wavebands in the visible range. Fig. 5 presents a time series of perturbed IOPs at 490 nm in ensembles with individual perturbations throughout 2017, in the

425 ~~Eastern~~ eastern part of the basin and at shallow depth (10.6 m). For absorption, we note that the spread around CDOM is the largest, in agreement with the high uncertainty set for CDOM IOPs that are not explicitly modelled in BAMHBI. Scattering coefficients are 10 to 100 times larger than absorption coefficients, while backscattering is about 10 times lower. Fig. 7 below illustrates how the perturbation of these coefficients ~~influence~~ influences the irradiance streams in E4, highlighting that most of the light is converted into the downward diffuse part E_s.

430

In the eastern gyre, CDOM has no clear seasonality. It dominates absorption throughout the year, with lower values at the end of summer and fall. (Back-)scattering is mainly dominated by non-algal particles except at the end of the year when phytoplankton reaches a similar and even larger contribution. Overall, we identify three different regimes throughout the year. In spring, we observe high biological activity associated with a phytoplankton bloom. Absorption is mostly dominated by CDOM, with high phytoplankton contribution, while scattering is dominated by non-algal particles, as their concentration increases after the phytoplankton bloom. During summer, we observe a regime of low biological activity once the high concentrations of phytoplankton and particles start to decrease after the bloom. At this stage, CDOM dominates absorption, whereas backscattering is dominated by non-algal particles. During the autumn, the contribution of phytoplankton increases again until it reaches a level similar to that of CDOM and water for absorption. For scattering, both contributions from phytoplankton and particles gradually increase in autumn. It is worth noting that the introduction of perturbations in this setup allows for a change of the constituent dominating absorption or (back-)scattering. For instance during blooms, perturbing the model may create a switch from a domination of absorption by CDOM to a domination by phytoplankton, or conversely, when contributions are of similar magnitude in the deterministic simulation. These three regimes are valid for the deep sea. In coastal and shallow areas such as the Northwestern shelf, biological activity follows different patterns. There, the contributions of phytoplankton and particles remain high throughout the year, with a lower contribution of CDOM to absorption. On the shelf, scattering and backscattering are mostly dominated by non-algal particles. However, in this paper, we focus on the deep central areas of the basin, as it is where the CDOM forcing is the most reliable.

Fig. 6 presents the seasonal cycle of the surface reflectance $R_{RS}(490)$ and $rCHL$ (as defined in Eq. 8) generated by the ensembles. Perturbations in backscattering and absorption influence the upward diffuse irradiance (see Fig. 7) which in turn modifies surface reflectance. Although backscattering directly influences the fractions of light scattered upward in the E_u stream, absorption is also of significant importance as it drives the ability of the water column to propagate irradiance streams. For instance with low absorption, the thickness of the surface layer in which backscattered light eventually reaches back to the surface increases. In spring, perturbations of chlorophyll and CDOM generate the largest dispersion (Fig. 6a). Low biological activity in summer leads to reduced dispersion in ensembles E1, E2 and E3, until it increases again in fall and triggers the dispersion of members. Perturbing the IOPs of non-algal particles seems to only have a limited influence on $rCHL$, and the perturbations remain significant in their influence on surface reflectance.

Although CDOM shows a large spread at 490 nm, it has little influence on reflectance at 555 nm, as its contribution to absorption is lower at longer wavelengths. On the other hand, the perturbation of contributions from phytoplankton and non-algal particles has a greater influence on reflectance at 555 nm. We also notice that some members drift from the deterministic run or from the ensemble mean. For instance in the E1 ensemble (perturbation of phytoplankton IOPs), one member (in grey) reaches high values for $rCHL$ during the diatom bloom while reflectance values at 490 nm remain rather close to that
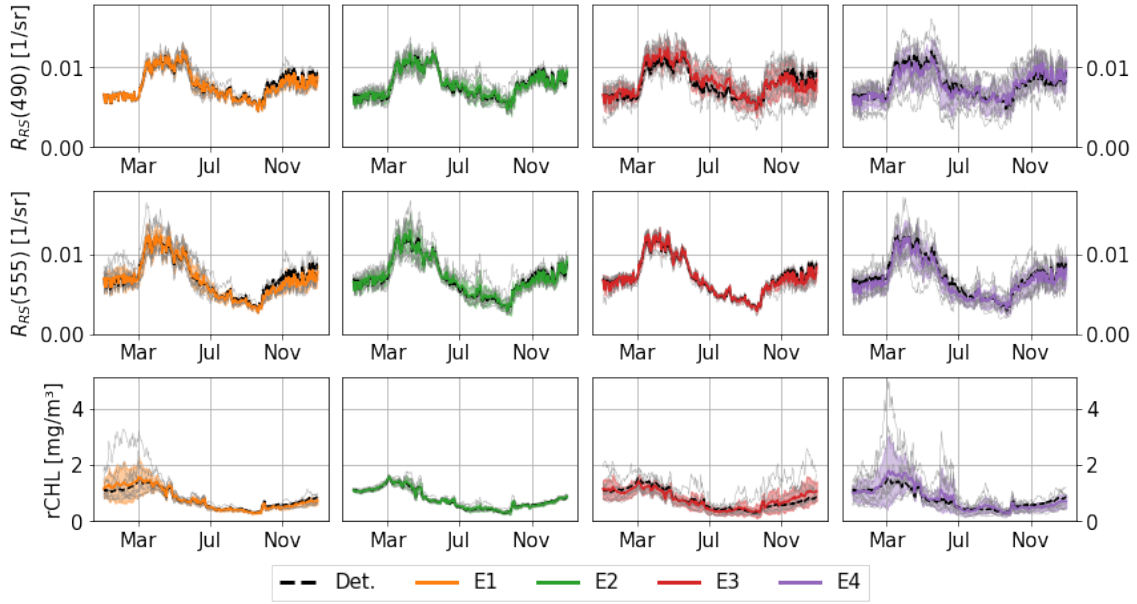
Figure 6. Time series of sea surface reflectance at 490 nm ($R_{RS}(490)$) and reflectance derived chlorophyll (~~rCHL~~ $rCHL$) over 2017 at the location 43.22N, 36.63E. For each ensemble, the standard deviation is represented with a shaded area. Phytoplankton, non-algal particles and CDOM IOPs are respectively perturbed in E1 (in orange), E2 (in green) and E3 (in red). All IOPs except pure water are perturbed in E4 (in purple). Each thinner grey line represents an individual member of the ensemble.

those of the other members. In this case, it is associated ~~to~~ with higher absorption at 555 nm that lowers the backscattered signal. In all ~~experiments,~~ of the experiments, the ensemble means remain rather close to the deterministic run, showing that no significant bias is introduced with the ensemble.

4.2 Combined vs individual perturbations

470 The different regimes evidenced with individual perturbations are also highlighted in the E4 ensemble with combined perturbations. The evolution of reflectance and ~~rCHL~~ $rCHL$ (Fig. 6~~d~~) simulated by the E4 ensemble exhibits ~~similar patterns as~~ patterns similar to those observed in the E1, E2 and E3 ensembles. For surface reflectance, early in the year, the spread of the E4 ensemble is only slightly larger than that of the E3 ensemble ~~(Fig. 6c)~~ at 490 nm in which only ~~CDOM optical properties~~ the optical properties of CDOM are perturbed. During ~~the~~ spring bloom, the spread in E4 becomes larger ~~resulting from~~ as the

475 result of a combined effect of CDOM (E3), phytoplankton (E1) and non-algal particles (E2). Similarly in summer, and despite the low dispersion observed in E1 and E2, the spread in E4 is greater than ~~in~~ with individual perturbations suggesting the influence of non-linearities. CDOM contributes the most to the uncertainty of R_{RS} at 490 nm which is consistent with its higher absorption power in shorter wavelengths. At 555 nm, CDOM contributes less to absorption with ~~higher~~ a greater influence of phytoplankton and non-algal particles. The seasonal evolution of ~~rCHL~~ $rCHL$ (right-hand side panels of Fig. 6) simulated by

480 E4 suggests a dominance of phytoplankton early in the year with ~~a~~ lower contribution of CDOM ~~in~~ the ensemble spread. The extent of the spread is much higher in E4 during the spring bloom than in E1 or E3, exhibiting again the ~~non linear~~ non-linear character of the perturbations and amplification by the model non-linear dynamics. In both E1 and E4, one member of each ensemble ~~shows very high values of rCHL~~ presents much higher values of $rCHL$ compared to the ensemble mean, thus largely increasing the spread of the ensemble. In summer, perturbations in CDOM and phytoplankton dominate the E4 spread with a

485 lower influence of non-algal particles. In autumn, CDOM perturbations dominate again the spread of ~~rCHL~~$rCHL$.

Fig. 7 shows the effect of combined perturbations of absorption and (back-)scattering coefficients on the three streams of irradiance in the eastern gyre of the Black Sea in early summer. The influence of perturbations is represented with both the ensemble mean in dotted lines and with the standard deviation of the ensemble. This figure shows that CDOM dominates

490 absorption at depth at 490 nm, consistently with the results presented in Fig. 5. (Back-)scattering gradually ~~increase~~ increases with depth and is dominated by phytoplankton and particles that result from a former bloom, with also a significant contribution of water to backscattering at surface. Below ~~2-3m~~ 2-3 m the downward diffusion stream largely dominates the other two streams and penetrates waters below 40 m. The direct downward stream E_d at 490 nm is fully absorbed after 5 to 7 m, mostly by CDOM, and (back-)scattered by phytoplankton and non-algal particles. The upward backscattered stream E_u, that

495 contributes to the reflectance, is the smallest one and is present up to around 30 m.

Most of the simulated variability in the total stream E_{total} occurs at low depths and ~~mainly results from~~ is mainly due to the variability in the scattered stream E_s. The impact of the uncertainty in IOPs on ~~the~~ direct and backscattered irradiances (E_d and E_u) is lower in magnitude due to lower absorption and backscattering coefficients. In this example, the combined effect

500 of perturbations results in an increase of the total absorption (i.e. the ensemble mean is larger than the deterministic solution over the whole column) while for (back-)scattering it is opposite. This results in a lower ensemble mean irradiance compared to the deterministic simulation close to the surface, while the backscattered E_u stream is also lower (Fig. 7a). The uncertainty ~~on the~~ in total light increases with depth and below 20 m has a spread comparable to the average light. At depth, this range is consistent with higher chlorophyll-a dynamics. For comparison, ~~standard deviation on~~ the standard deviation of E_{total} is 21%

505 at 10 m depth and 53% at 30 m depth.

~~Figure~~ Fig. 8 presents the spread of the upward diffuse irradiance E_u at 490 nm at the surface simulated over the whole Black Sea in summer in the ~~4~~ four ensemble experiments. Since the incident irradiance is the same in all ensembles, the difference in E_u results only from the perturbation of IOPs. It shows that ~~CDOM perturbation~~ the perturbation of CDOM has the largest

510 influence on E_u, which subsequently ~~influence~~ influences sea surface reflectance. ~~While~~ Although CDOM does not backscatter light, it absorbs the three streams including E_u (Eq. 3). ~~Perturbation~~ The perturbation of phytoplankton IOPs has the second largest influence, with non-algal particles having the least influence. Their contribution is two-fold: directly on backscattering and through absorption. ~~Standard~~ The standard deviations and ensemble means are summarised in Table 5. It is worth noting
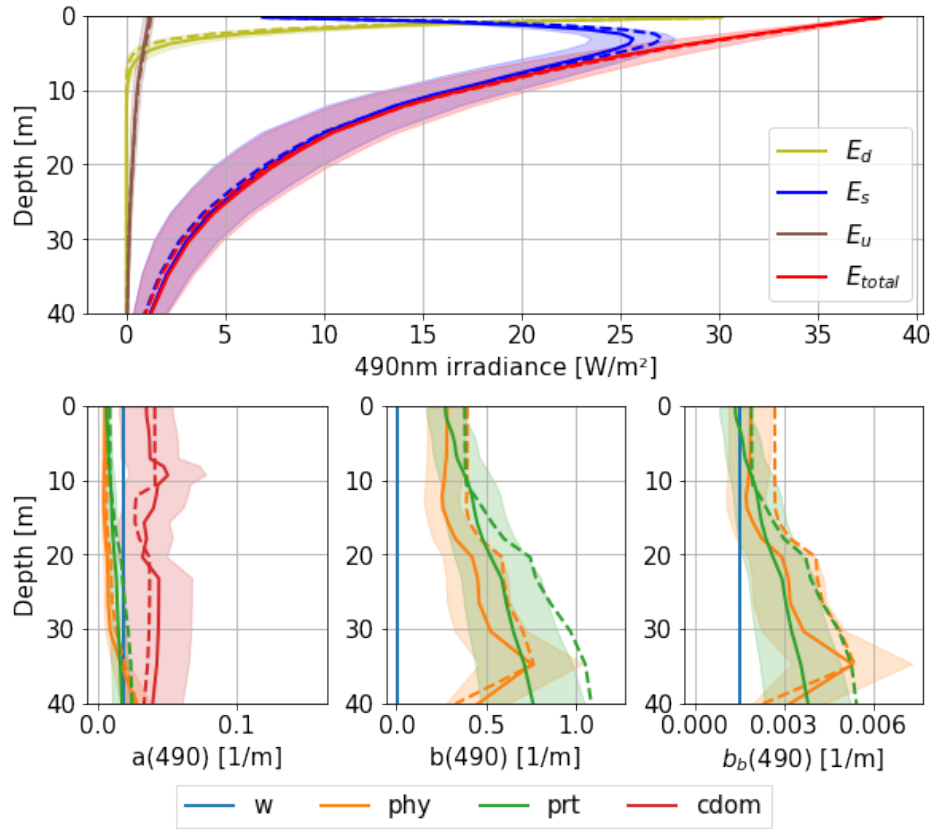
Figure 7. Irradiance (top) and IOP (bottom) profiles at 490 nm. Profiles are taken here at 43.22N, 36.63E on 23rd June 2017, at solar zenith. Solid lines represent the ensemble mean with shaded areas representing standard deviation of the ensemble. Dotted lines represent the deterministic run.

that the ensemble means are kept close to 1, again showing that no bias is introduced with the perturbations.

515

~~The effect of combined perturbations in E4 is shown in~~ In Fig. 8~~d.~~, E4 shows greater extrema in the ensemble than E1, E2 and E3, but the standard deviation of E_u remains rather close to that of E3 where only the CDOM was perturbed, with 20.7% for E4. The amplitude of the combined perturbation is therefore lower than the sum of amplitudes of individual perturbations, exhibiting the non-linearity of this relationship. The increase in spread still shows that perturbations are amplified when com-

520 bined and do not cancel out each other. It ~~is also worth noting~~ should also be noted that the standard deviation ~~with~~ for each ensemble is lower than the 50% standard deviation used to generate perturbations.
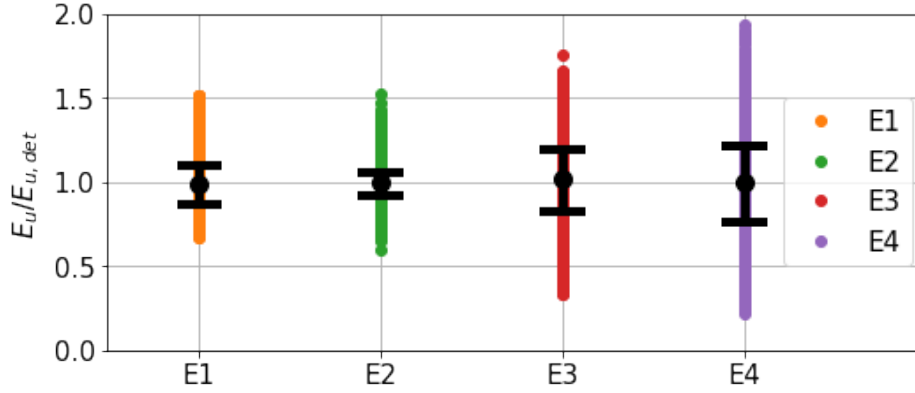
Figure 8. ~~E_u~~ Distributions of $E_u(490)$ at ~~490 nm distribution at~~ sea surface normalised by its deterministic value, for the whole basin on 23rd June 2017 and each experiment. Circles and black lines represent the ensemble mean and standard deviation.

E_u	at 490 nm Ensemble mean	Standard deviation
E1	0.985	11.4%
E2	0.993	6.5%
E3	1.013	18.8%
E4	0.996	20.7%

Table 5. Ensemble statistics for normalised upward irradiance fields E_u/E_u^{ref}

4.3 Comparison to observations

In this subsection, we assess the quality of the E4 ensemble by comparing the distribution of ~~the~~ simulated irradiance and reflectance fields with observations.

4.3.1 BGC-ARGO profiles

A collection of 108 BGC-Argo profiles from floats 6901866 and 7900591, collected ~~over the year~~ during 2017 in the ~~Eastern~~ eastern gyre of the Black Sea, is used to compare the ensemble E4 ~~to~~ with *in situ* observations. As we want to assess the representation of marine optics within the water column regardless of the surface forcing, we normalise the irradiance profiles by ~~the~~ their surface values. PAR data from BGC-Argo floats is given in units of μmol/s/m². The conversion to W/m², the unit used in the model outputs, is performed using 1 W/m² = 4.6 μmol/s/m² to obtain comparable quantities. This approximation is given for daylight conditions in Thimijan and Heins (1983). In sunny conditions, this coefficient would normally have to be lower. Fig. 9 shows the average normalised profiles of the simulated and measured downwelling irradiance at 490 nm and PAR. The downwelling irradiance E_{down} is here defined as the sum of the direct and scattered irradiance streams E_d and E_s. It shows that while there is ~~a~~ good agreement close to the surface for both variables, divergences appear at depths greater than
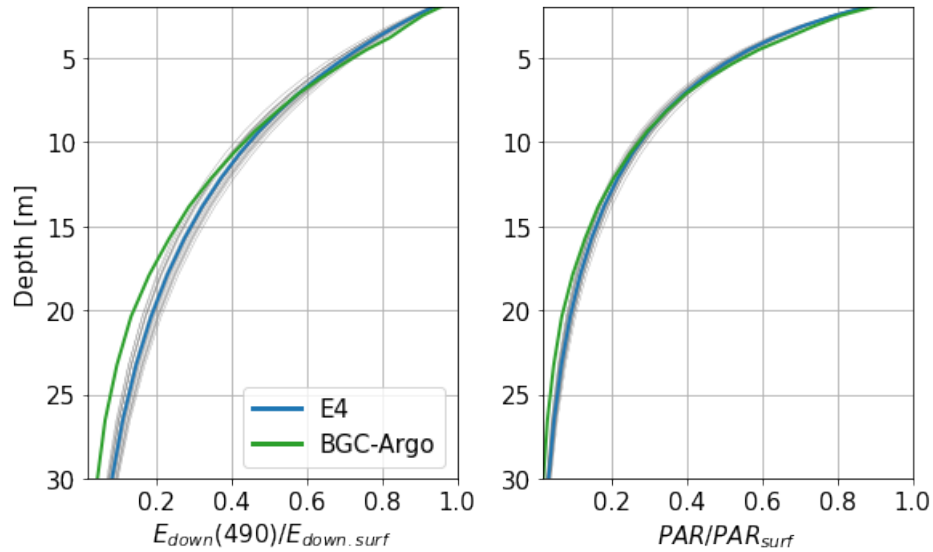
Figure 9. Profiles of downwelling irradiance E_{down} at 490 nm and PAR from BGC-Argo data and the E4 ensemble normalised by their surface values. Each thinner grey line represents an individual member of the ensemble.

15 m. This result, while expected since the calibration of CDOM optics was performed on the same type of data, illustrates that the RT model is able to represent the total amount of light in a way that is consistent with *in situ* data at shallow depths. Below 15 m, when the ~~divergence start to occur~~signals begin to diverge, about 70% of the irradiance has already been absorbed.

540 ~~Comparison~~The comparison to BGC-Argo measurements ~~reveal~~reveals a rather strong agreement between observed irradiance profiles and their equivalent computed by the RT model, although not all of the observed profiles fall within the ensemble spread throughout the year. Fig. 10 shows the time series of ~~$E_d(490)$~~$E_{down}(490)$ and PAR at 10.6 m depth, both directly and normalised by their surface values. ~~While~~Although the observations remain contained within the ensemble spread during winter and spring, the ensemble then overestimates the irradiance and PAR (i.e., does not absorb enough) during early sum-
545 mer. ~~It is worth noting that some~~ For PAR data, part of the discrepancies in summer could be explained by inconsistent unit conversion in sunny conditions. Some residual error can likely be attributed to the BGC-Argo measurements (e.g. sensor drift, sensitivity to temperature)~~and explain some of the discrepancies observed in this comparison~~, in particular close to the surface. The agreement is then better during the early autumn, still with an overestimation in the final months of the year. This appears more clearly in the normalised profiles where the biases appear distinctly in summer and at the end of the year. We also notice
550 some outliers in the observations that seem to indicate isolated events of underestimated irradiance, but those data points may indicate local fine-scale variations that are not captured, or observation error.
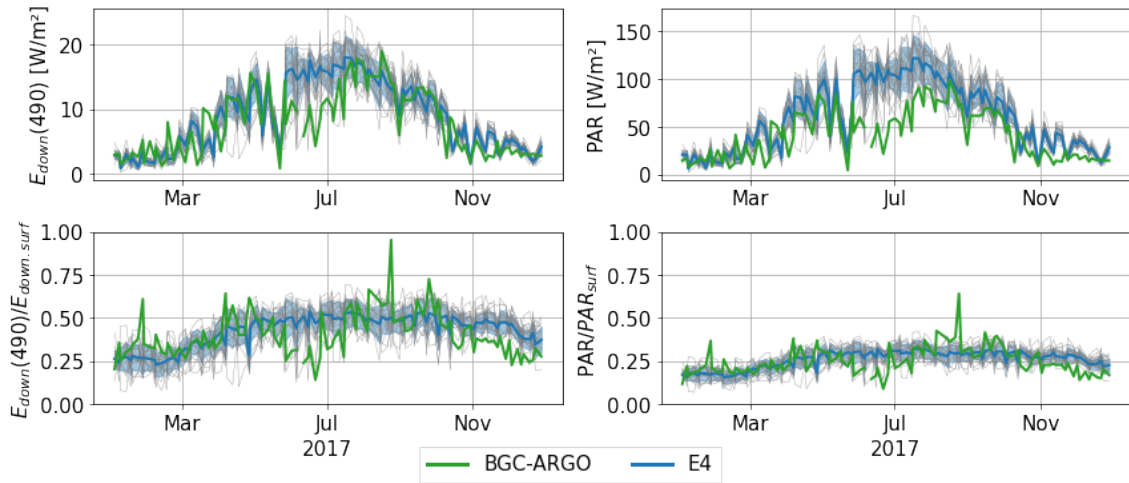
Figure 10. Time series over 2017 of downwelling irradiance (i.e. $E_d + E_s$) at 490 nm (top left) and PAR (top right) at 10.6 m depth for the E4 ensemble and BGC-Argo data from floats 6901866 and 7900591. They are also shown normalised with their surface value (bottom). Floats here both drift in the Eastern part of the basin during this period. Each thin grey line represents an ensemble member. The standard deviation of the ensemble is represented with the shaded blue area.

~~While~~ Although part of the data remains outside ~~of~~ the ensemble spread, it seems that the ensemble is able to capture most of the measurements from BGC-Argo data. Fig. 11 shows a rank histogram ~~gathering~~ that gathers the normalised data from the time series in Fig. 10 illustrating the dispersion of the observation data within the ensemble members. A rank histogram (Candille and Talagrand, 2004) aims at assessing the reliability of an ensemble. ~~It sorts observations within the~~ A rank is attributed to each observation, that is equal to its relative position among the realisations of the ensemble for this observation. The entire set of observations is ranked within the sorted ensemble of corresponding simulated data. A flat histogram evidences perfect reliability, i.e. an ensemble distribution that matches the distribution of observations. ~~Each observation is ranked within the sorted ensemble, with the extreme ranks corresponding~~ A convex rank histogram suggests that the ensemble is over-dispersive (all observations tend to be within the ensemble), while a concave rank histogram suggests that the ensemble is under-dispersive (observations tend to be outside of the ensemble). The extreme ranks correspond to observations that are lower or higher than all realisations of the ensemble. To compute this histogram, we consider an observation error of 6% on the normalised irradiance measured by the BGC-Argo floats. This value is that prescribed for the satellite products (information from manufacturer - https://biogeochemical-Argo.org/measured-variables-general-context.php).

~~A large number of~~ Some observations are not captured by the ensemble (Fig. 11), suggesting ~~an under-dispersed ensemble . At lower depths,~~ that the ensemble is under-dispersed. Fig. 9 ~~showed that the ensemble overestimates irradiance and PAR~~ shows that despite excellent agreement close to the surface (also evidenced in Fig. 10), irradiance tends to be slightly overestimated deeper in the water column, regardless of the perturbation. ~~The ensemble therefore does not seem able to fully capture the~~
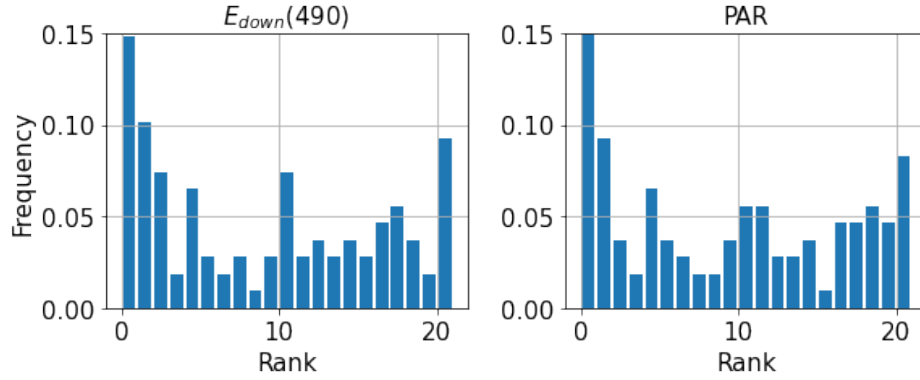
Figure 11. Rank histograms using BGC-Argo data in 2017 for ~~$E_d(490$~~ $E_{down}(490)$ (left) and PAR (right), at 10.6 m depth. Observations are sorted within the E4 ensemble.

Nonetheless, the ensemble is close to representing the distribution of measured irradiance streams. It is worth mentioning that the ~~amount~~ number of observations may not be sufficient here to provide a full picture of the reliability of the ensemble. ~~While~~ Although it provides an overview of the ability of the model to reproduce the distribution of downwelling irradiance, the greater amount of observations provided by satellite data offers a ~~bigger~~ larger dataset to assess the ensemble skill.

4.3.2 Remote-sensed data

Comparison with remote-sensed data allows ~~a~~ for better coverage of the basin both spatially and temporally. We start by studying the temporal signature ~~from~~ of the ensemble by comparing time series of reflectance in the ~~Eastern~~ eastern gyre at 490 and 555 nm, and ~~rCHL~~$rCHL$. Fig. 12 shows that the simulated reflectances are higher than observations for most of the year ~~at~~ with the exception of the summer period where higher reflectances are sensed by satellite instruments. These ~~correspond most likely~~ likely correspond to a coccolitophore bloom (Kubryakov et al., 2021), ~~whose backscattering~~ of which the magnitude is largely underestimated in the model. This underestimation of reflectance by the model is observed for both the 490 and 555 nm wavebands. Interestingly, the chlorophyll from remote-sensed reflectance does not peak during the coccolithophore bloom event. The bias is greatly reduced in the estimation of ~~rCHL. Indeed~~$rCHL$. Indeed, as this quantity is a ratio between reflectances in two wavebands that are rather close, uncertainties on measurement and corrections such as the BRDF coefficient partly cancel out. However, we still observe a clear overestimation ~~by~~ in the model during winter and early spring. From June and until the end of the year, observations are captured by the ensemble at this location of the eastern gyre.

To better characterise the quality of the ensemble of ~~rCHL~~$rCHL$ outputs, we compute the rank histograms over the whole basin at three dates selected in winter (~~March~~ 5th March), end of spring (~~June~~ 8th June) and end of summer (~~September~~ 13th September) during days with limited cloud cover for better satellite coverage over the whole basin. The observation error used to generate ~~those~~ these rank histograms is set to 30%, as in Popov et al. (2024). Fig. 13 presents the resulting rank histograms
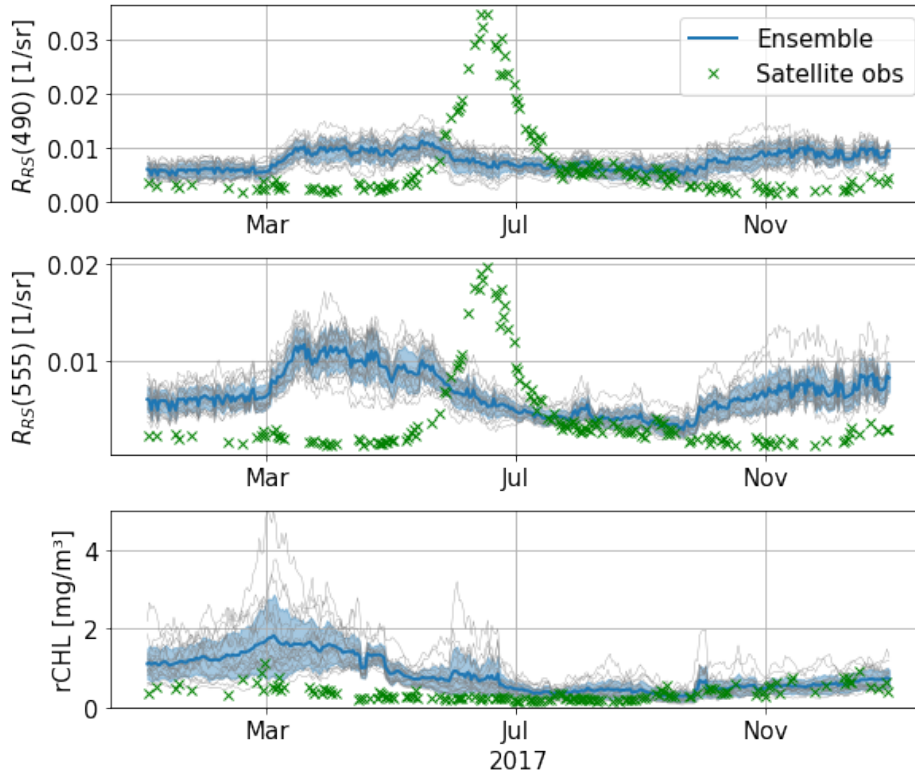
Figure 12. Time series over 2017 of R_{RS} at 490 (top) and 555 nm (centre), and reflectance-derived chlorophyll (bottom). Series are taken in the eastern gyre (43.22N, 36.63E). The standard deviation of the ensemble is represented in shaded blue and each thin grey line corresponds to a member of the ensemble.

and the associated maps. Rank maps show the spatial distribution of observation ranks. In this representation, we discard coastal and shallow areas, as these are more complex waters where the ocean colour algorithm described in section 2.5 shows weak performances. ~~Then, only~~ Only areas of the basin with a depth greater than 150 m are therefore considered.

595

Fig. 13 shows the spatial and temporal ~~localisation~~ location of the bias in ~~rCHL~~$rCHL$. It confirms the presence of the bias in the beginning of the year ~~as on March~~ such as on the 5th ~~, with only~~ of March, with few observations that are captured by the ensemble in the South of the Black Sea. In June, the bias seems to decrease with a greater ~~amount~~ number of observations that are captured by the ensemble in the ~~Eastern~~ eastern part of the basin. This is confirmed on the rank histogram that presents

600 a lower peak and better distributed data. ~~The data remains however~~ However, data remains gathered on the left side of the rank histogram, exhibiting an overestimation of ~~rCHL~~ $rCHL$ by the ensemble. The bias there seems to be mainly located at the periphery of the gyres, ~~while~~ whereas observations close to the centre of both gyres appear to be better captured. In September, the flatter rank histogram shows that the model captures the observations in a more consistent way. We may still observe a
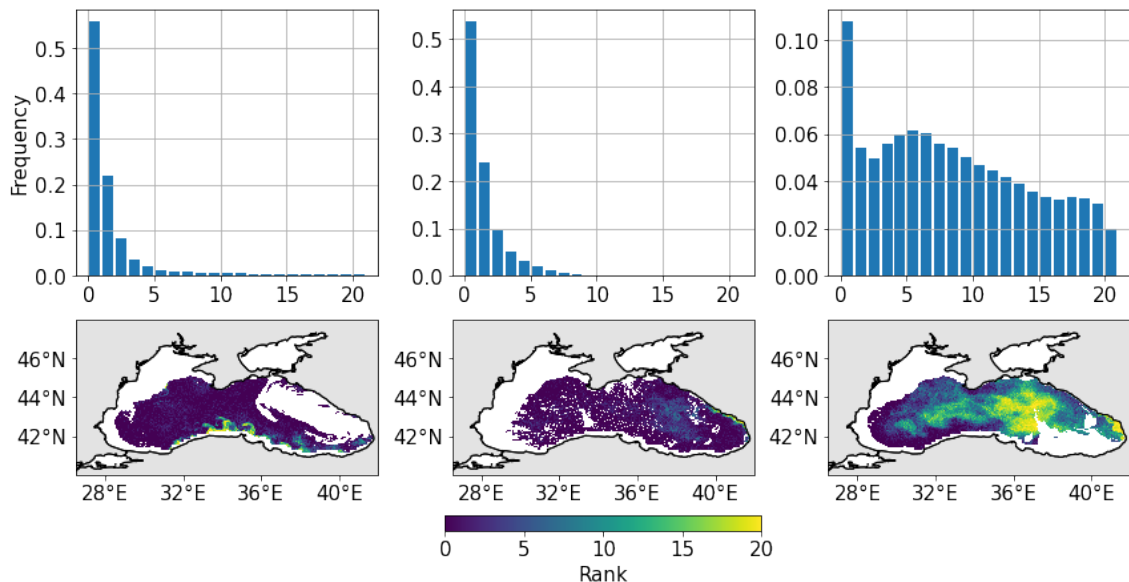
Figure 13. Rank histograms and maps for ~~rCHL~~ $rCHL$ on 5th March (left), 8th June (centre) and 13th September (right).

positive bias in the Southwestern parts of the basin, but ~~the~~ central areas are consistently represented.

605

Finally, we proceed to a more complete comparison between the chlorophyll estimated by the satellite and the BGC-Argo with that predicted by the BAMHBI model and estimated from the reflectance ~~rCHL~~ $rCHL$. We subsample model and satellite surface chlorophyll data at the times and locations of BGC-Argo measurements. For the BGC-Argo and BAMHBI deterministic run, surface chlorophyll is defined as the average concentration over the top 10 m, which corresponds to the average water optical depth in the Black Sea (Peneva and Stips, 2005). The resulting time series are presented in Fig. 14.

610

Despite the bias observed in ~~rCHL~~ $rCHL$ in the first months of the year, surface chlorophyll derived from reflectance appears to be closer to observations than the chlorophyll computed by the biogeochemical model. In winter, both estimates of chlorophyll overestimate its concentration, but the deviation is lower with ~~rCHL. Both methods then~~ $rCHL$. Then, both methods provide similar estimates in spring before exhibiting contrasting results in summer and autumn with a slight overestimation for ~~rCHL and~~ $rCHL$ and an underestimation for BAMHBI chlorophyll. In the last months of the year, both estimates remain close to observations. Despite the use of BAMHBI chlorophyll as an optical component that governs the ~~light propagation~~ propagation of light and then the surface reflectance from which ~~is derived rCHL~~ $rCHL$ is derived, both signals do not seem to always follow similar patterns throughout the year, even during blooms. This highlights the role of the other constituents when biological activity is high. We also note that the *in situ* BGC-Argo data is rather consistent with the remote-sensed data.

615

620
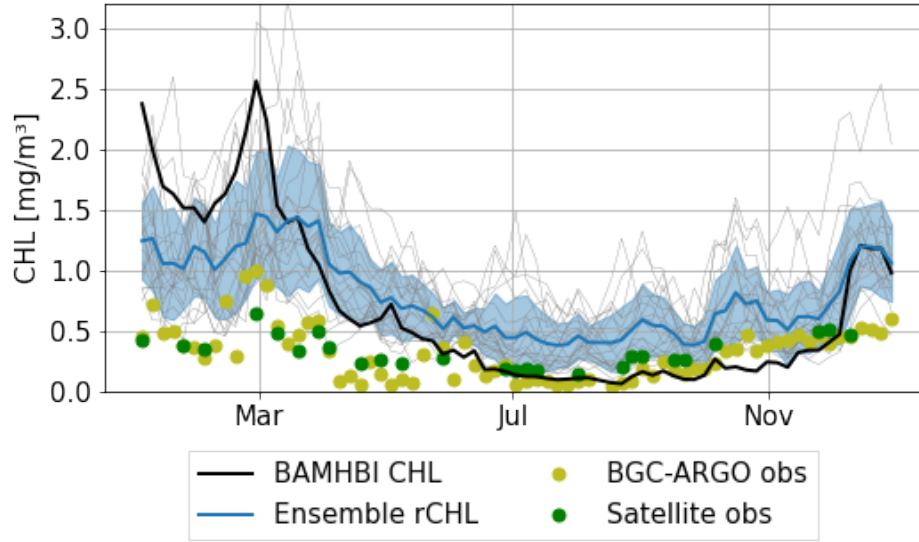
Figure 14. Surface chlorophyll estimated by BGC-Argo, satellite~~and~~, the biogeochemical model (dynamically simulated by BAMHBI) and estimated from reflectance (~~rCHL~~$rCHL$). Comparisons are shown at times and locations of BGC-Argo measurements in 2017, along ~~Argo~~ BGC-Argo float 6901866.

5 Discussion

In this section, we first analyse the quality of the generated ensemble to represent the variability in the observations ~~. We then summarise~~ before summarising the main impacts of ~~IOPs~~ IOP uncertainties on the simulated radiative fields. Limitations of the approach are discussed, and the potential of using radiometric data to better constrain biogeochemical models is discussed based on our results.

5.1 Quality of the ensemble

~~By taking~~ Taking uncertainties into account in the formulation of the RT model, we produce ensemble distributions of irradiance and ~~rCHL~~ $rCHL$ that provide enriched information ~~with respect~~ compared to a single deterministic simulation. To test the quality of the ~~ensembles~~ensemble, we assess the consistency of the simulated distribution of irradiance and reflectance-derived chlorophyll (~~rCHL~~$rCHL$) with remote-sensed and *in situ* observations. The ensemble E4 that combines all the perturbations under-disperses the distribution of the downwelling irradiance at 490 nm and PAR when compared to BGC-Argo data, with an increasing bias observed with depth.

From the analysis of surface reflectance distributions, we notice that the consistency of the ensemble generated ~~rCHL~~ $rCHL$ with satellite data varies ~~across~~ throughout the year. The ensemble shows good agreement from the end of spring until late autumn in most parts of the basin (excluding shallow areas such as the continental shelf). ~~Rank~~ The rank histograms (Fig. 13)

~~evidence~~ show that the distribution of ~~rCHL~~ $rCHL$ is closer to that of observations in the second half of the year. In winter and early spring, the consistency of the ensemble data with observations is lower and observations are not captured. ~~This is indeed the~~ In fact, this is the time period during which the deterministic biogeochemical model strongly overestimates chlorophyll as measured by satellites. Further calibration of the biogeochemical model or better ~~parameterisation~~ parametrisation of its uncertainties, including from other sources that were not accounted for, is needed ~~in~~ under those conditions to first improve the deterministic solution.

It should be noted that this analysis is essentially valid in the surface layer and the visible spectral range. Comparison to BGC-Argo profiles ~~show~~ shows a mismatch at depth over 15 m (Fig. 9), where about 30% of the incident irradiance is still propagating downward. There, the current ~~parameterisation~~ parametrisation of absorption may be lacking to accurately represent irradiance profiles. The uniformity of perturbations applied on the vertical also does not allow to account for an inaccurate depth of phytoplankton maximum for instance, that has a significant influence on the propagation of irradiance in lower depths. ~~Results obtained at~~ The results obtained at the surface remain close to the observations and confirm the benefits of using ensemble methods to describe uncertain processes and parameters such as IOPs.

5.2   Influence of uncertainties in IOPs on radiative fields

As shown in the ~~times~~ time series in Fig. 5, CDOM has the greatest influence on absorption in the blue end of the visible spectrum, and less so at 555 nm. Phytoplankton and non-algal particles dominate scattering and backscattering with seasonal variations in their relative dominance imprinted by the bloom dynamics. With depth, all contributions increase as concentrations of phytoplankton, non-algal particles and CDOM gradually increase. The direct irradiance stream E_d only penetrates a few metres ~~because of~~ due to the high scattering properties of ~~water constituents~~ the water components, as seen in Fig. 7. Below, the light field is strongly dominated by the downward diffuse stream E_s. The upward stream E_u is always of smaller magnitude and almost null below 25 m. The spread in the vertical light field is mostly due to the downward diffuse stream. As a consequence of uncertainties in ~~the~~ absorption and (back-)scattering, its spread increases with depth and below 10 m has a magnitude that can impact photosynthesis and then the amplitude of the deep chlorophyll maximum. This effect is ~~however~~ not tested here since the light generated by the RT model is not used to force the biogeochemical model.

As presented in Fig. 7 with a_{cdom} for instance, we sometimes observe a mean effect that deviates the ensemble mean from the deterministic results. This is likely caused by model non-linearities such as the S_{cdom} coefficient in the formulation of a_{cdom}, and despite the introduction of perturbations that do not create bias in the perturbed IOPs. It could also be noted that this effect could be mitigated by increasing the ensemble size, ~~that~~ which could explain deviations in (back-)scattering coefficients. ~~Overall~~ In general, combining perturbations increases the spread of the ensemble compared to single perturbations as ~~exhibited~~ shown in Fig. 8. The non-linear character of the model however leads to lower spreads in E4 than the simple sum of spreads with individual perturbations. In all ~~4 ensembles,~~ four ensembles, the spreads in irradiance and reflectance remain

lower than the 50% standard deviations used to perturb the IOPs.

5.3 Importance of CDOM

CDOM largely dominates the absorption at short wavelengths (lower than 500 nm) and strongly influences the propagation of the three light streams. Since CDOM is not explicitly simulated by the biogeochemical model, we assume its uncertainty to be the largest. The comparison of ensembles shows that the ensemble that combines the different sources of perturbations has similar patterns to that obtained with CDOM perturbations, only with a wider spread. The high influence of CDOM perturbation on the outputs of the RT model shows how important this component is and what variations its inaccurate estimation can generate. Perturbing CDOM has a strong influence on E_u and therefore on R_{RS}. Unfortunately, most biogeochemical models either strongly oversimplify or do not explicitly solve CDOM dynamics. The reasons are the lack of knowledge and data to parametrise CDOM, although its inclusion in models was proven relevant (Terzić et al., 2019). In our study, CDOM is represented as a forcing derived from BGC-Argo data. This approach has limitations since BGC-Argo floats do not cover the shallow areas of the basin. In order to link CDOM seasonal and spatial variability to ocean physics, the CDOM forcing is scaled by seawater density, with CDOM being parametrised as an increasing function of density as described in section 2.4.3. However, this procedure results in low CDOM values in low density areas that do not match the reality of coastal areas largely influenced by river discharges. Although the perturbation of CDOM absorption accounts for the uncertainty that arises from the method used to derive its forcing, the large variations that could be observed in coastal areas are likely not captured by the ensemble due to the different biogeochemical mechanisms at play. These results highlight the need for better representation of CDOM in biogeochemical models to successfully model RT in shorter wavelengths and provide a more complete assessment of the spatial and temporal variability of CDOM IOPs.

5.4 Limitations of the approach

The optically active components considered here are the three phytoplankton functional groups simulated in BAMHBI, non-algal particles and CDOM. The results of this study are influenced by the way these components are modelled in the biogeochemical model. First, as described above, the forcing used to represent CDOM absorption has its limitations, especially near shallow areas. We also ignore suspended minerals that can also be optically important, limiting the accuracy of our study on the continental shelf (Stramski et al., 2016). Moreover, as in Dutkiewicz et al. (2015), the size of particles is assumed to be uniform, which is an oversimplification. The modelling of phytoplankton optics is also largely influenced by the PFTs simulated in the model, that are representative of diatoms, dinoflagellates and small flagellates. This last group mainly integrates coccolithophores, although BAMHBI does not consider calcification. The analysis of reflectance fields clearly shows that the model misses the reflectance peaks in June associated with the coccolithophore

bloom. During this period, BAMHBI simulates a bloom of small flagellates but its optical signature is underestimated. This arises both from a flawed parametrisation of IOPs and from an underestimation of the bloom in BAMHBI. We could also investigate the inclusion of more PFTs that are relevant for the Black Sea, such as diazotrophs (Dechenne, 2023) or synechococcus (Uysal, 2001).

There are still improvements to be made in the current formulation of the stochastic RT model based on the current variables provided by BAMHBI. Several challenges remain in calibrating the deterministic RT model properly due to the rather limited amount of optical *in situ* data in the Black Sea, as well as the composition of phytoplankton. The addition of stochastic processes as described in this paper only allows to account for model uncertainty up to a certain extent. For instance, the perturbations applied here do not influence the depth of optically active constituents. This would likely need to be perturbed too, if we seek to explain discrepancies with observations. With the current method, a phytoplankton bloom that is too deep in the model will not see its depth perturbed. In this study, we also chose to only perturb the RT model with no feedback towards the hydrodynamical and biogeochemical models (i.e. the modified light field is not that used in the coupled model). By considering it and other sources of uncertainty, such as surface radiation, that affect biological processes, we may be able to capture some of the observations that remain outside of the ensemble E4 spread and provide a more complete description of the sensitivity of the RT model.

5.5 Radiometric observations to constrain coupled physical-biogeochemical models

The analysis performed with this RT model also paves the way to use radiometric quantities for calibration, validation and assimilation in a physical-biogeochemical model in the Black Sea. Comparison to reflectance data still shows high biases that would require prior corrections, but the definition of reflectance ratios, or associated variables such as reflectance-derived chlorophyll ($rCHL$), shows promising results. Band ratios remove some of the uncertainties associated with corrections.

This study also provides a better understanding of the strengths and limitations of ocean colour algorithms. While those algorithms aim at estimating surface chlorophyll concentrations, the ocean colour products fundamentally remain optical quantities that are compared to biogeochemical variables in models. Based on colour, the use of the blue/green band ratio algorithm does not only "see" chlorophyll, but also other types of in-water material. As such, reflectance-derived chlorophyll proves itself to be closer to the satellite-retrieved chlorophyll than the chlorophyll computed in BAMHBI. Currently, ocean colour products are being assimilated in biogeochemical models that rarely resolve reflectance. This study hints at the opportunities provided by working directly with ocean colour derived from reflectances, that accounts for more than just chlorophyll and therefore may be closer to the true meaning of such estimates. It also suggests that the assimilation of satellite surface reflectances has the potential to correct the IOPs and ultimately improve the simulation of irradiance streams and reflectances.

6 Conclusion and perspectives

The modelling of light in the coupled physical-biogeochemical NEMO-BAMHBI framework for the Black Sea is enriched by
adding a spectral radiative transfer model that explicitly solves the upward and downward light field at high spectral resolution.
This offers a direct connection between model variables and remote-sensed reflectance data, without relying on inversion algorithms. Four optically important water constituents are considered: pure water, phytoplankton, non-algal particles and CDOM.
We aim at assessing the relative contribution of each constituent while accounting for the uncertainties in their IOPs using
ensemble simulations. CDOM clearly dominates absorption at short wavelengths throughout the year while phytoplankton and
non-algal particles dominate the (back-)scattering, having the largest influence during and following algal blooms.

As it is not explicitly simulated in BAMHBI, we assume higher uncertainty on CDOM IOPs than phytoplankton and non-algal particles. ~~Ensemble show that~~ The ensembles show that the perturbation of CDOM has a dominant influence on the
radiative fields. Its major role highlights the need for a better representation of this component in our biogeochemical model,
which will require high quality data in the Black Sea. Such data ~~are~~ is currently practically non-existent in the central areas and
shelf zone, thus hampering modelling capabilities.

The quality of the generated ensembles is assessed by comparing the ensemble distributions of irradiances, reflectances and
reflectance-derived chlorophyll (~~rCHL~~$rCHL$) with observations. We find that the distributions generated by the ensemble do
not capture all the spatial and temporal variability in the measurements performed in the Black Sea. This is particularly the
case in coastal areas, and during winter and important blooms. This suggests that the introduction of uncertainties on IOPs is
not enough to fully account for uncertainties in the RT model. First, vertical perturbations that could influence the position of
the deep chlorophyll maximum are missing ~~,~~ and could be added to simulate uncertainties more realistically. Other sources
need to be considered, such as forcings or ~~parameterisation~~ parametrisation of the hydrodynamics and biogeochemistry. Their
influence has been studied in other frameworks such as in Garnier et al. (2016).

Comparison to remote-sensed data shows promising agreement on reflectance ratios, even though the reflectances themselves are less accurately modelled. Uncertainties on the atmospheric correction or interface effects (e.g. BRDF) are indeed
removed using reflectance ratios between close wavebands. We also ~~evidence that rCHL~~ show that $rCHL$ provide estimates of
chlorophyll that are closer to remote-sensed data than the chlorophyll modelled in BAMHBI based on biological mechanisms.
Using reflectances could then allow to better characterise errors in the model.

Finally, in this paper, the coupling between the physical-biogeochemical model and the RT model is ~~in~~ one-way. ~~It~~ This
means that the chlorophyll and non-algal particles simulated by BAMHBI are used to compute the IOPs in the RT model, but
the light field produced by the RT model is not used to compute temperature and photosynthetic active radiation. Rather, a
simple one-stream optical model differentiating three ~~wavelength~~ wavelengths is used to force the physical-biogeochemical
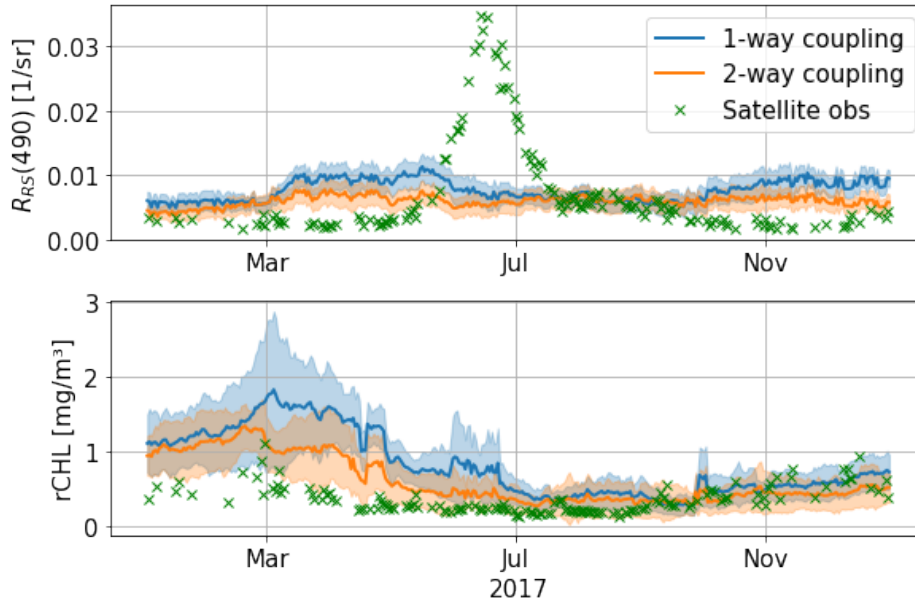
Figure 15. Time series of $R_{RS}(490)$ (~~left~~top) and ~~rCHL~~ $rCHL$ (~~right~~bottom) at 43.22N, 36.63E with the 1-way (E4, in blue) and 2-way (in ~~brown~~orange) configurations.

model. We test a two-way configuration that, despite biases in the simulated radiative fields, shows promising results. The simulated time series of $R_{RS}(490)$ and ~~rCHL are in better agreement~~ $rCHL$ agree better with satellite data (Fig. 15). We find that in this ~~2-way~~ two-way configuration, the irradiance feedback towards the coupled framework does not disrupt the simulation of reflectance, although ~~decreasing~~ it decreases $R_{RS}(490)$ to bring it closer to satellite observations. For ~~rCHL~~ $rCHL,$ however, this first outlook shows that we are able to better compare remote-sensed data with this 2-way configuration, especially in the first months of the year. A two-way configuration for the coupled framework NEMO-BAMHBI-RT model will possibly pave the way towards the explicit assimilation of ~~multi-spectral~~ multispectral satellite reflectance in coupled physical-biogeochemical ocean models.

780   *Data availability.* Ocean colour data was taken from Black Sea, Bio-Geo-Chemical, L3, daily Satellite Observations (1997-ongoing). E.U. Copernicus Marine Service Information (CMEMS). Marine Data Store (MDS). DOI: 10.48670/moi-00303 (Accessed on 05-03-2024). BGC-Argo data were collated within the Copernicus Marine Service (In Situ) and EMODnet collaboration framework. Data is made freely available by the Copernicus Marine Service and the programs that contribute to it. DOI: 10.13155/59938; 10.13155/43494 (Accessed on 06-12-2023).

Appendix A: Generation of a_{cdom} forcing

CDOM is a major contributor to absorption in seawater, but is not explicitly simulated in the NEMO-BAMHBI framework. Therefore, we cannot use the same approach as for phytoplankton and non-algal particles. We choose here to derive a forcing for a_{cdom} from the *in situ* BGC-Argo data. A collection of 625 profiles from floats 6901866 and 6903240 provide measurements of irradiance in 3 wavebands (E_{Argo} at 380, 412 and 490 nm), chlorophyll concentration (chl_{Argo}), backscattering coefficient at 700 nm ($bbp_{700,Argo}$) and CDOM ($cdom_{Argo}$). Some profiles are discarded ~~according to the quality flags of~~ depending on the quality control flag for variables of interest~~here~~. Float 6901866 has measurements between June 2015 and June 2019 in the entire basin with limited coverage of the central parts. Float 6903240 has measurements between April 2018 and July 2022, mostly around the Western Gyre. Both floats do not cover the continental shelf, where the dynamics of CDOM are more complex.

In the RT model, we parametrise the IOPs of phytoplankton and non-algal particles from biogeochemical variables of BAMHBI. We use the same ~~parameterisation~~ parametrisation to derive a_{cdom}. We choose a reference wavelength $\lambda_{ref} = 412$ nm in the range of high CDOM absorption and with irradiance profiles measured by BGC-Argo floats to derive a reference a_{cdom} profile. We use the RT model to simulate the same profiles that are measured. IOPs of water are known in the same way as described in Section 2.4.1. IOPs of phytoplankton are derived ~~by~~ using chlorophyll profiles from BGC-Argo data instead of BAMHBI variables. However, we cannot discriminate between PFTs and therefore assume that chlorophyll is equally distributed between the 3 PFTs solved in BAMHBI. The IOPs of non-algal particles are derived from profiles of particulate backscattering coefficient at 700 nm $bbp_{700,Argo}$. We assume this coefficient to be the sum of contributions from phytoplankton and non-algal particles to derive a POC concentration that is ~~consistent with our parameterisation~~ used to apply our parametrisation:

$$POC_{Argo} = \frac{bbp_{700,Argo} - b_{b.phy}(700)}{b_{b,prt}^0(700)} \tag{A1}$$

We assume that the optical properties of CDOM on a water column are a linear function of CDOM concentration, i.e. that on a water column, all CDOM has the same absorbing power. We want a_{cdom} profiles to have the same shape as CDOM profiles measured by BGC-Argo float. We therefore assume:

$$a_{cdom} = k_{cdom} cdom_{Argo} \tag{A2}$$

with k_{cdom} unknown. Starting with an initial value of $k = 1\,m^{-1}$, ~~We then compute~~ we then compute the downwelling irradiance stream $E_{loop}(\lambda_{ref})$ for all profiles and compare them with the BGC-Argo irradiance profiles. For each profile, the parameter k is then updated to minimise the difference between the $E_{loop}(\lambda_{ref})$ and $E_{Argo}(\lambda_{ref})$ profiles on the top 30m of the ocean (21 model layers), normalised by their surface value for consistency in assessing the influence of IOPs. This simple optimisation problem is written:
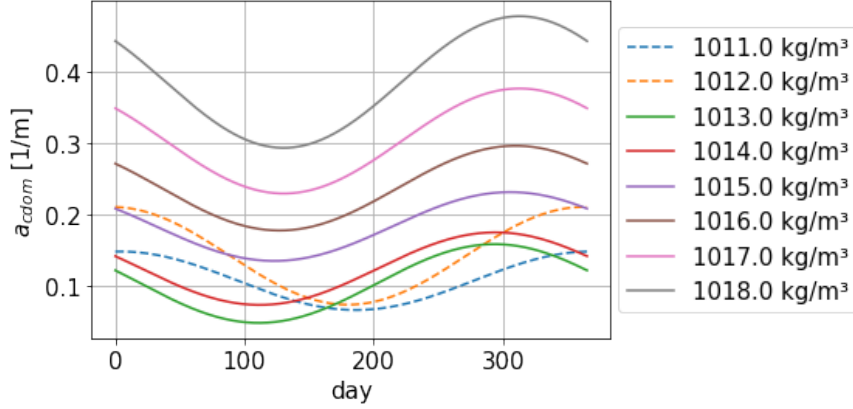
Figure A1. a_{cdom} forcing scaled in density for $\lambda_{ref} = 412$ nm. This forcing was generated using a collection of BGC-Argo profiles in the deeper areas of the Black Sea.

$$815 \quad min \sum_{k=1}^{21} \left(\frac{E_{loop}(\lambda_{ref})}{E_{loop}(\lambda_{ref})^{surf}} - \frac{E_{Argo}(\lambda_{ref})}{E_{Argo}(\lambda_{ref})^{surf}} \right) \tag{A3}$$

We use a deviation threshold of 2% to accept a ~~k value~~ value of k for a given profile. Using this method for each profile of our collection, we get a new collection of k_{Argo} and then of $a_{cdom}(\lambda_{ref})$ profiles. We now store values of $a_{cdom}(\lambda_{ref})$ according to time and seawater density ~~as~~ to link each time and location of the basin to a value ~~for~~ of $a_{cdom}(412)$. We interpolate this dataset to generate annual cycles for each density scale ~~in order to smoothen~~ to smooth out the forcing. Fig. A1 shows the
820   resulting forcing for $a_{cdom}(\lambda_{ref})$ for selected seawater densities.

Appendix B: Model performance in the visible spectral range

In this paper, we focus on the wavebands that are used to derive ~~rCHL~~$rCHL$, centred on 490 and 555 nm, respectively in the blue and the green. More generally, we computed irradiance and sea surface reflectance in the 6 wavebands that are found in
825   the multi-satellite reflectance product for the Black Sea made available by the Copernicus Marine Service, centred on 412, 443, 490, 510, 555 and 670 nm. Fig. B1 shows the average spectral sea surface reflectance in the eastern gyre of the Black Sea over 2017. As seen previously in the 490 and 555 nm centred wavebands, the model tends to overestimate sea surface reflectance. The model reflectance is consistent with remote-sensed data up to around 475 nm, after which the bias gradually increases for longer wavelengths. The deviation then decreases at the near infrared end of the spectral range.
830   ~~R_{RS} average spectra in the eastern gyre over 2017. Uncertainties in model and remote-sensed data are represented in shaded areas.~~
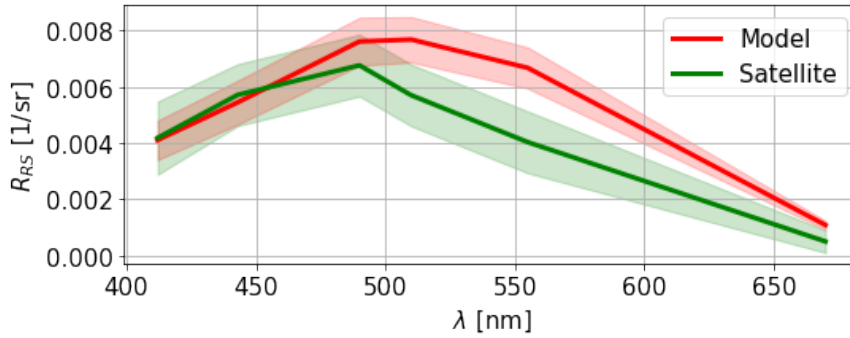
Figure B1. R_{RS} average spectra in the eastern gyre over 2017. Uncertainties in model and remote-sensed data are represented in shaded areas.

Author contributions. LM, PB and MG conceptualised the research plan. LV completed the initial integration of the radiative transfer model into the NEMO-BAMHBI framework. LV and MG provided support with the NEMO-BAMHBI model. JMB and PB provided support with ensemble methods within the NEMO framework. LM performed the model calibration and ensemble simulations, analysis and wrote the first draft of the paper. All authors contributed to reviewing and editing the paper until its final version. MG provided funding through the BRIDGE-BS and NECCTON projects.

Competing interests. The authors declare that they have no conflict of interest.

Acknowledgements. This work was funded by the EU H2020 BRIDGE-BS project under grant agreement no. 101000240 and the EU HE NECCTON project under grant agreement no. 101081273. Insights from the ODESSA, MEDIATION and POSYDONIE projects were brought by the coauthors. Computational resources have been provided by the Consortium des Équipements de Calcul Intensif (CÉCI), funded by the Fonds de la Recherche Scientifique de Belgique (F.R.S.-FNRS) under Grant No. 2.5020.11 and by the Walloon Region. We thank S. Dutkiewicz for sharing the MITGCM Darwin radiative transfer code. We also thank , and P. Lazzari, M. Baklouti, J. Lamouroux and P. Verezemskaya for helpful discussions . and suggestions. We also thank two anonymous reviewers for their comments and suggestions that contributed to improving this article.

845 References

Aas, E.: Two-stream irradiance model for deep waters, Appl. Optics, 26, 2095–2101, https://doi.org/10.1364/ao.26.002095, 1987.

Ackleson, S., Balch, W., and Holligan, P.: Response of water-leaving radiance to particulate calcite and chlorophyll a concentrations: A model for Gulf of Maine coccolithophore blooms, J. Geophys. Res., 99, 7483–7499, https://doi.org/10.1029/93JC02150, 1994.

Álvarez, E., Lazzari, P., and Cossarini, G.: Phytoplankton diversity emerging from chromatic adaptation and competition for light, Prog.
850   Oceanogr., 204, https://doi.org/10.1016/j.pocean.2022.102789, 2022.

Álvarez, E., Cossarini, G., Teruzzi, A., Bruggeman, J., Bolding, K., Ciavatta, S., Vellucci, V., D'Ortenzio, F., Antoine, D., and Lazzari, P.: Chromophoric dissolved organic matter dynamics revealed through the optimization of an optical–biogeochemical model in the north-western Mediterranean Sea, Biogeosciences, 20, 4591–4624, https://doi.org/10.5194/bg-20-4591-2023, 2023.

Aumont, O., Ethé, C., Tagliabue, A., Bopp, L., and Gehlen, M.: PISCES-v2: an ocean biogeochemical model for carbon and ecosystem
855   studies, Geosci. Model Dev., 8, 2465–2513, https://doi.org/10.5194/gmd-8-2465-2015, 2015.

Baird, M. E., Wild-Allen, K. A., Parslow, J., Mongin, M., Robson, B., Skerratt, J., Rizwi, F., Soja-Wozniak, M., Jones, E., Herzfeld, M., Margvelashvili, N., Andrewartha, J., Langlais, C., Adams, M. P., Cherukuru, N., Gustafsson, M., Hadley, S., Ralph, P. J., Rosebrock, U., Schroeder, T., Laiolo, L., Harrison, D., and Steven, A. D. L.: CSIRO Environmental Modelling Suite (EMS): scientific description of the optical and biogeochemical models (vB3p0), Geosci. Model Dev., 13, 4503–4553, https://doi.org/10.5194/gmd-13-4503-2020, 2020.

860 Bissett, W., Carder, K., Walsh, J., and Dieterle, D.: Carbon cycling in the upper waters of the Sargasso Sea: II. Numerical simulation of apparent and inherent optical properties, Deep-Sea Res. Pt. I, 46, 271–317, https://doi.org/10.1016/S0967-0637(98)00063-6, 1999.

Brankart, J.-M., Candille, G., Garnier, F., Calone, C., Melet, A., Bouttier, P.-A., Brasseur, P., and Verron, J.: A generic approach to explicit simulation of uncertainty in the NEMO ocean model, Geosci. Model Dev., 8, 1285–1297, https://doi.org/10.5194/gmd-8-1285-2015, 2015.

Butenschön, M., Clark, J., Aldridge, J., Allen, J., Artioli, Y., Blackford, J., Bruggeman, J., Cazenave, P., Ciavatta, S., Kay, S., Lessin,
865   G., van Leeuwen, S., van der Molen, J., de Mora, L., Polimene, L., Sailley, S., Stephens, S., and Torres, R.: ERSEM 15.06: a generic model for marine biogeochemistry and the ecosystem dynamics of the lower trophic levels, Geosci. Model Dev., 9, 1293–1339, https://doi.org/10.5194/gmd-9-1293-2016, 2016.

Cahill, B., Schofield, O., Chant, R., Wilkin, J., Hunter, E., Glenn, S., and Bissett, P.: Dynamics of turbid buoyant plumes and the feedbacks on near-shore biogeochemistry and physics, Geophys. Res. Lett., 35, https://doi.org/10.1029/2008GL033595, 2008.

870 Cahill, B., Kowalczuk, P., Kritten, L., Gräwe, U., Wilkin, J., and Fischer, J.: Estimating the seasonal impact of optically significant water constituents on surface heating rates in the western Baltic Sea, Biogeosciences, 20, 2743–2768, https://doi.org/10.5194/bg-20-2743-2023, 2023.

Candille, G. and Talagrand, O.: Evaluation of probabilistic prediction systems for a scalar variable, Q. J. Roy. Meteor. Soc., 131, 2131–2150, https://doi.org/10.1256/qj.04.71, 2004.

875 Capet, A.: Study of the multi-decadal evolution of the Black Sea hydrodynamics and biogeochemistry using mathematical modelling, Ph.D. thesis, ULiège - Université de Liège, https://hdl.handle.net/2268/163502, 2014.

Ciavatta, S., Torres, R., Martinez-Vicente, V., Smyth, T., Dall'Olmo, G., Polimene, L., and Allen, J. I.: Assimilation of remotely-sensed optical properties to improve marine biogeochemistry modelling, Prog. Oceanogr., 127, 74–95, https://doi.org/10.1016/j.pocean.2014.06.002, 2014.

880 Dechenne, A.: Black Sea and diazotrophs, toward an improvement of modeling the nitrogen cycle, Master's thesis - Université de Liège, https://matheo.uliege.be/handle/2268.2/18590, 2023.

Dutkiewicz, S., Hickman, A., Jahn, O., Gregg, W., Mouw, C., and Follows, M.: Capturing optically important constituents and properties in a marine biogeochemical and ecosystem model, Biogeosciences, 12, 4447–4481, https://doi.org/10.5194/bg-12-4447-2015, 2015.

Dutkiewicz, S., Hickman, A., and Jahn, O.: Modelling ocean-colour-derived chlorophyll a, Biogeosciences, 15, 613–630, https://doi.org/10.5194/bg-15-613-2018, 2018.

Fujii, M., Boss, E., and Chai, F.: The value of adding optics to ecosystem models: a case study, Biogeosciences, 4, 817–835, https://doi.org/10.5194/bgd-4-1585-2007, 2007.

Gallegos, C., Werdell, P., and McClain, C.: Long-term changes in light scattering in Chesapeake Bay inferred from Secchi depth, light attenuation, and remote sensing measurements, J. Geophys. Res., 116, https://doi.org/10.1029/2011JC007160, 2011.

Gallée, H., Trouvilliez, A., Agosta, C., Genthon, C., Favier, V., and Naaim-Bouvet, F.: Transport of Snow by the Wind: A Comparison Between Observations in Adélie Land, Antarctica, and Simulations Made with the Regional Climate Model MAR, Bound.-Lay. Meteorol., 146, 133–147, https://doi.org/10.1007/s10546-012-9764-z, 2013.

Garnier, F.: Paramétrisations stochastiques de processus biogéochimiques non résolus dans un modèle couplé NEMO/PISCES de l'Atlantique Nord, PhD Thesis, 2016.

Garnier, F., Brankart, J.-M., Brasseur, P., and Cosme, E.: Stochastic parameterizations of biogeochemical uncertainties in a 1/4° NEMO/PISCES model for probabilistic comparisons with ocean color data, J. Marine Syst., 155, 59–72, https://doi.org/10.1016/j.jmarsys.2015.10.012, 2016.

Grailet, J.-F., Hogan, R., Ghilain, N., Bolsée, D., Fettweis, X., and Grégoire, M.: Inclusion of the ECMWF ecRad radiation scheme (v1.5.0) in the MAR (v3.14), regional evaluation for Belgium, and assessment of surface shortwave spectral fluxes at Uccle, Geosci. Model Dev., 18, 1965–1988, https://doi.org/10.5194/gmd-18-1965-2025, 2025.

Gregg, W. and Casey, N.: Skill assessment of a spectral ocean–atmosphere radiative model, J. Marine Syst., 76, 49–63, https://doi.org/10.1016/j.jmarsys.2008.05.007, 2009.

Gregg, W. and Rousseaux, C.: Directional and Spectral Irradiance in Ocean Models: Effects on Simulated Global Phytoplankton, Nutrients, and Primary Production, Front. Mar. Sci., 3:240, https://doi.org/10.3389/fmars.2016.00240, 2016.

Grégoire, M. and Soetart, K.: Carbon, nitrogen, oxygen and sulfide budgets in the Black Sea: A biogeochemical model of the whole water column coupling the oxic and anoxic parts, Ecol. Model., 221, 2287–2301, https://doi.org/10.1016/j.ecolmodel.2010.06.007, 2010.

Grégoire, M., Raick, C., and Soetart, K.: Numerical modeling of the central Black Sea ecosystem functioning during the eutrophication phase, Prog. Oceanogr., 76, 286–333, https://doi.org/10.1016/j.pocean.2008.01.002, 2008.

Grégoire, M., Alvera-Azcarate, A., Buga, L., Capet, A., Constantin, S., D'Ortenzio, F., Doxaran, D., Faugeras, Y., Garcia-Espriu, A., Golumbeanu, M., Gonzalez-Haro, C., Gonza´lez-Gambau, V., Kasprzyk, J.-P., Ivanov, E., Mason, E., Mateescu, R., Meulders, C., Olmedo, E., Pons, L., Pujol, M.-I., Sarbu, G., Turiel, A., Vandenbulcke, L., and Rio, M.-H.: Monitoring Black Sea environmental changes from space: New products for altimetry, ocean colour and salinity. Potentialities and requirements for a dedicated in-situ observing system, Front. Mar. Sci., 9, https://doi.org/10.3389/fmars.2022.998970, 2023.

Hogan, R. and Bozzo, A.: A Flexible and Efficient Radiation Scheme for the ECMWF Model, J. Adv. Model. Earth Sy., 10, 1990–2008, https://doi.org/10.1029/2018MS001364, 2018.

Hogan, R. and Matricardi, M.: A Tool for Generating Fast k-Distribution Gas-Optics Models for Weather and Climate Applications, J. Adv. Model. Earth Sy., 14, https://doi.org/10.1029/2022MS003033, 2022.

Jones, E. M., Baird, M. E., Mongin, M., Parslow, J., Skerratt, J., Lovell, J., Margvelashvili, N., Matear, R. J., Wild-Allen, K., Robson, B., Rizwi, F., Oke, P., King, E., Schroeder, T., Steven, A., and Taylor, J.: Use of remote-sensing reflectance to constrain a data assimilating marine biogeochemical model of the Great Barrier Reef, Biogeosciences, 13, 6441–6469, https://doi.org/10.5194/bg-13-6441-2016, 2016.

Kajiyama, T., D'Alimonte, D., and Zibordi, G.: Algorithms Merging for the Determination of Chlorophyll-a Concentration in the Black Sea, IEEE Geosci. Remote S., 16, 677–681, https://doi.org/10.1109/LGRS.2018.2883539, 2018.

Kettle, H. and Merchant, C.: Modeling ocean primary production: sensitivity to spectral resolution of attenuation and absorption of light, Prog. Oceanogr., 78, 135–146, https://doi.org/10.1016/j.pocean.2008.04.002, 2008.

Kitidis, V., Stubbins, A., Uher, G., Upstill Goddard, R., Law, C., and Woodward, E.: Variability of chromophoric organic matter in surface waters of the Atlantic Ocean, Deep-Sea Res. Pt. II, 53, 1666–1684, https://doi.org/10.1016/j.dsr2.2006.05.009, 2006.

Kubryakov, A., Mikaelyan, A., and Stanichny, S.: Extremely strong coccolithophore blooms in the Black Sea: The decisive role of winter vertical entrainment of deep water, Deep-Sea Res. Pt. I, 173, https://doi.org/10.1016/j.dsr.2021.103554, 2021.

Lee, Z., Carder, K., and Arnone, R.: Deriving inherent optical properties from water color: a multi-band quasi-analytical algorithm for optically deep waters, Appl. Optics, 41, 5755–5772, https://doi.org/10.1364/AO.41.005755, 2002.

Lengaigne, M., Menkes, C., Aumont, O., Gorgues, T., Bopp, L., André, J.-M., and Madec, G.: Influence of the oceanic biology on the tropical Pacific climate in a coupled general circulation model, Clim. Dynam., 28, 503–516, https://doi.org/10.1007/s00382-006-0200-2, 2007.

Manizza, M., Le Quéré, C., Watson, A., and Buitenhuis, E.: Bio-optical feedbacks among phytoplankton, upper ocean physics and sea-ice in a global model, Geophys. Res. Lett., 32, L05 603, https://doi.org/10.1029/2004GL020778, 2005.

Mason, J., Cone, M., and Fry, E.: Ultraviolet (250–550 nm) absorption spectrum of pure water, Appl. Optics, 55, https://doi.org/http://dx.doi.org/10.1364/AO.55.007163, 2016.

Mobley, C.: Fast light calculations for ocean ecosystem and inverse models, Opt. Express, 19, 18 927–18 944, https://doi.org/10.1364/oe.19.018927, 2011.

Mobley, C., Chai, F., Xiu, P., and Sundman, L.: Impact of improved light calculations on predicted phytoplankton growth and heating in an idealized upwelling-downwelling channel geometry, J. Geophys. Res.-Oceans, 120, 875–892, https://doi.org/10.1002/2014JC010588, 2015.

Morel, A.: Optical properties of pure water and pure sea water, Optical Aspects of Oceanography, 19, 1–24, 1974.

Morel, A., Antoine, D., and Gentili, B.: Bidirectional reflectance of oceanic waters: accounting for Raman emission and varying particle scattering phase function, Appl. Optics, 41, 6289–6306, https://doi.org/10.1364/AO.41.006289, 2002.

Morel, A., Claustre, H., Antoine, D., and Gentili, B.: Natural variability of bio-optical properties in Case 1 waters: attenuation and reflectance within the visible and near-UV spectral domains, as observed in South Pacific and Mediterranean waters, Biogeosciences, 4, 913–925, https://doi.org/10.5194/bg-4-913-2007, 2007.

Peneva, E. and Stips, A.: Numerical Simulations of Black Sea and Adjoined Azov Sea, Forced with Climatological and Meteorological Reanalysis Data, Tech. Rep. EUR 21504 EN, CEC JRC, Institute of Environment and Sustainability, https://doi.org/10.13140/RG.2.1.1830.4722, 2005.

Pope, R. and Fry, E.: Absorption spectrum 380 –700 nm of pure water. II. Integrating cavity measurements, Appl. Optics, 36, https://doi.org/10.1364/ao.36.008710, 1997.

Popov, M., Brankart, J.-M., Capet, A., Cosme, E., and Brasseur, P.: Ensemble analysis and forecast of ecosystem indicators in the North Atlantic using ocean colour observations and prior statistics from a stochastic NEMO–PISCES simulator, Ocean Sci., 20, 155–180, https://doi.org/10.5194/os-20-155-2024, 2024.

Silkin, V., Mikaelyan, S., Pautova, L., and Fedorov, A.: Annual Dynamics of Phytoplankton in the Black Sea in Relation to Wind Exposure, J. Mar. Sci. Eng., 9, 1435, https://doi.org/10.3390/jmse9121435, 2021.

Skákala, J., Bruggeman, J., Ford, D., Wakelin, S., Akpinar, A., Hull, T., Kaiser, J., Loveday, B., O'Dea, E., Williams, C., and Ciavatta, S.: The impact of ocean biogeochemistry on physics and its consequences for modelling shelf seas, Ocean Model., 172, https://doi.org/10.1016/j.ocemod.2022.101976, 2022.

Stanev, E. and Beckers, J.-M.: Barotropic and baroclinic oscillations in strongly stratified ocean basins: Numerical study of the Black Sea, J. Marine Syst., 19, 65–112, https://doi.org/10.1016/S0924-7963(98)00024-4, 1999.

Stramski, D., Bricaud, A., and Morel, A.: Modeling the Inherent Optical Properties of the Ocean Based on the Detailed Composition of the Planktonic Community, Appl. Optics, 40, 2929–2945, https://doi.org/10.1364/AO.40.002929, 2016.

Terzić, E., Lazzari, P., Organelli, E., Solidoro, C., Salon, S., D'Ortenzio, F., and Conan, P.: Merging bio-optical data from Biogeochemical-Argo floats and models in marine biogeochemistry, Biogeosciences, 16, 2527–2542, https://doi.org/10.5194/bg-16-2527-2019, 2019.

Terzić, E., Miró, A., Organelli, E., Kowalczuk, P., D'Ortenzio, F., and Lazzari, P.: Radiative transfer modeling with biogeochemical Argo float data in the Mediterranean Sea, J. Geophys. Res.-Oceans, 126, https://doi.org/10.1029/2021JC017690, 2021.

Thimijan, R. and Heins, R.: Photometric, Radiometric, and Quantum Light Units of Measure: A Review of Procedures for Interconversion, Hortic. Sci., 18, 818–822, https://doi.org/http://dx.doi.org/10.21273/HORTSCI.18.6.818, 1983.

Twardowski, M., Boss, E., Sullivan, J., and Donaghay, P.: Ocean Color Analytical Model Explicitly Dependent on the Volume Scattering Function, Mar. Chem., 89, 69–88, https://doi.org/10.3390/app8122684, 2004.

Uysal, Z.: Chroococcoid cyanobacteria Synechococcus spp. in the Black Sea: pigments, size, distribution, growth and diurnal variability, J. Plankton. Res., 23, 175–190, https://doi.org/10.1093/plankt/23.2.175, 2001.

Werdell, P., McKinna, L., Boss, E., Ackleson, S., Craig, S., Gregg, W., Lee, Z., Maritorena, S., Roesler, C., Rousseaux, C., Stramski, D., Sullivan, J., Twardowski, M., Tzortziou, M., and Zhang, X.: An overview of approaches and challenges for retrieving marine inherent optical properties from ocean color remote sensing, Prog. Oceanogr., 160, 186–212, https://doi.org/10.1016/j.pocean.2018.01.001, 2018.

Zibordi, G., Mélin, F., Berthon, J.-F., and Talone, M.: In situ autonomous optical radiometry measurements for satellite ocean color validation in the Western Black Sea, Ocean Sci., 11, 275–286, https://doi.org/10.5194/os-11-275-2015, 2015.